

c2d *SPITZER* IRS SPECTRA OF DISKS AROUND T TAURI STARS. I. SILICATE EMISSION AND GRAIN GROWTH

JACQUELINE KESSLER-SILACCI,¹ JEAN-CHARLES AUGEREAU,^{2,3} CORNELIS P. DULLEMOND,⁴ VINCENT GEERS,² FRED LAHUIS,^{2,5}
NEAL J. EVANS II,¹ EWINE F. VAN DISHOECK,² GEOFFREY A. BLAKE,⁶ A. C. ADWIN BOOGERT,⁷
JOANNA BROWN,⁷ JES K. JØRGENSEN,⁸ CLAUDIA KNEZ,¹ AND KLAUS M. PONTOPPIDAN²

Received 2005 September 13; accepted 2005 November 2

ABSTRACT

Infrared $\sim 5\text{--}35\ \mu\text{m}$ spectra for 40 solar mass T Tauri stars and 7 intermediate-mass Herbig Ae stars with circumstellar disks were obtained using the *Spitzer Space Telescope* as part of the c2d IRS survey. This work complements prior spectroscopic studies of silicate infrared emission from disks, which were focused on intermediate-mass stars, with observations of solar mass stars limited primarily to the $10\ \mu\text{m}$ region. The observed 10 and $20\ \mu\text{m}$ silicate feature strengths/shapes are consistent with source-to-source variations in grain size. A large fraction of the features are weak and flat, consistent with micron-sized grains indicating fast grain growth (from 0.1 to $1.0\ \mu\text{m}$ in radius). In addition, approximately half of the T Tauri star spectra show crystalline silicate features near 28 and $33\ \mu\text{m}$, indicating significant processing when compared to interstellar grains. A few sources show large $10\text{--}20\ \mu\text{m}$ ratios and require even larger grains emitting at $20\ \mu\text{m}$ than at $10\ \mu\text{m}$. This size difference may arise from the difference in the depth into the disk probed by the two silicate emission bands in disks where dust settling has occurred. The $10\ \mu\text{m}$ feature strength versus shape trend is not correlated with age or $H\alpha$ equivalent width, suggesting that some amount of turbulent mixing and regeneration of small grains is occurring. The strength versus shape trend is related to spectral type, however, with M stars showing significantly flatter $10\ \mu\text{m}$ features (larger grain sizes) than A/B stars. The connection between spectral type and grain size is interpreted in terms of the variation in the silicate emission radius as a function of stellar luminosity, but could also be indicative of other spectral-type-dependent factors (e.g., X-rays, UV radiation, and stellar/disk winds).

Subject headings: circumstellar matter — infrared: ISM — ISM: lines and bands — solar system: formation — stars: formation — stars: pre-main-sequence

1. INTRODUCTION

Dust in disks can be quite different from dust in the interstellar medium (ISM). Observations and chemical modeling (Grossman 1972; Gail 1998) suggest that the dust in the early stages of star formation is primarily composed of small ($< 1\ \mu\text{m}$) amorphous silicates with strong features at approximately 9.7 and $18.5\ \mu\text{m}$ (for a summary, see Pollack 1984). Large modifications of the dust occur in the envelopes and disks around young stars, as the initially small grains are processed via collisions and coagulation. Spectral energy distributions (SEDs) indicate that grain growth, as well as the corresponding settling of large grains to the disk midplane, is occurring in some disks. Dust settling and growth affect disk temperatures and vertical structures, resulting in dust photospheres that are flatter rather than flared (e.g., D’Alessio et al. 1999; Chiang et al. 2001; Dullemond & Dominik 2004). In addition, some main-sequence stars show evidence of a “second

generation” of small grains in a debris disk, produced by the collision and fragmentation of planetesimals, that may be quite different from the “primordial” dust.

The spectroscopic study of silicate emission has proven a valuable tracer of grain processing within young circumstellar disks. This method probes small grains via optically thin emission from the surface layer of generally optically thick disks. Studies of $\sim 10\ \mu\text{m}$ silicate emission from Herbig Ae-Be stars (HAEBEs) and T Tauri stars (TTs) with disks show early evidence of the growth of these surface-layer grains from ~ 0.1 to $2.0\ \mu\text{m}$ (see, e.g., Bouwman et al. 2001; van Boekel et al. 2003). Detections of additional spectral features arising from crystalline silicate emission in some HAEBE and TT disks (Waelkens et al. 1996; Sitko et al. 1999; Meeus et al. 2001; Honda et al. 2003; Acke & van den Ancker 2004), the debris disk β Pic (e.g., Knacke et al. 1993), and comets (see the review by Wooden 2002) provide evidence for silicate processing during the disk phase. Although changes in grain size and composition are closely linked to disk properties and planet formation, the rate and mechanism of grain growth and processing in disks are still not well understood.

Previous studies of silicate emission from TT disks were primarily focused on the Si—O stretching mode feature near $10\ \mu\text{m}$, which can be observed from the ground. Grain growth and crystallization, however, have similar effects on the shape of the $10\ \mu\text{m}$ feature. In these previous studies, the presence of crystalline silicates was often established through the presence of flux at $11.3\ \mu\text{m}$, corresponding to an emission feature of the crystalline Mg-rich silicate forsterite, in addition to the presence of an amorphous olivine feature at $9.8\ \mu\text{m}$. The combined effect is a broad, trapezoidal silicate emission feature with a peak near $9.7\ \mu\text{m}$ and

¹ Department of Astronomy, University of Texas at Austin, 1 University Station C1400, Austin, TX 78712-0259; jes@astro.as.utexas.edu.

² Leiden Observatory, P.O. Box 9513, 2300 RA Leiden, Netherlands.

³ Laboratoire d’Astrophysique de l’Observatoire de Grenoble, B.P. 53, 38041 Grenoble Cedex 9, France.

⁴ Max-Planck-Institut für Astrophysik, P.O. Box 1317, D-85741 Garching, Germany.

⁵ SRON, P.O. Box 800, 9700 AV Groningen, Netherlands.

⁶ Division of Geological and Planetary Sciences, Mail Code 150-21, California Institute of Technology, Pasadena, CA 91125.

⁷ Division of Production Engineering, Machine Design, and Automation, Mail Code 105-24, California Institute of Technology, Pasadena, CA 91125.

⁸ Harvard-Smithsonian Center for Astrophysics, Mail Stop 42, 60 Garden Street, Cambridge, MA 02138.

a secondary peak near $11.3 \mu\text{m}$. If crystalline silicates are abundant, the feature can appear broader and flatter. In contrast, growth of amorphous olivines can mimic the effects of crystalline-amorphous silicate mixtures, resulting in weaker, “flat-topped” $10 \mu\text{m}$ silicate features, with similar flux at 9.8 and $11.3 \mu\text{m}$ (e.g., van Boekel et al. 2003; Przygodda et al. 2003; Kessler-Silacci et al. 2005). Indeed, the above studies showed that the flattened silicate features were well matched by models of purely amorphous olivines with grain sizes (radii) of $2 \mu\text{m}$. Therefore, evaluation of the grain size and/or crystallinity requires observations of a larger spectral region, in which the presence of distinct forsterite or enstatite features (and polycyclic aromatic hydrocarbons [PAHs], which emit near 7.7 , 8.5 , and $11.2 \mu\text{m}$) can be assessed. Complementary studies of the O—Si—O bending mode near $20 \mu\text{m}$ probe slightly cooler dust and, combined, give a better sense of the grain size and crystalline fraction in the disk.

Spectra covering a large spectral region, including several isolated crystalline silicate features (27.5 , 33.5 , 35.8 , and $70 \mu\text{m}$), were obtained for disks around HAEBEs (and some TTs) with the *Infrared Space Observatory* (*ISO*). *ISO* observations of several disks around intermediate-mass HAEBEs clearly established the presence/absence of crystalline silicates (see Molster & Waters [2003] and van Dishoeck [2004] for reviews). In addition, *ISO* observations probed the ~ 10 and $\sim 20 \mu\text{m}$ emission features from amorphous silicates in HAEBE disks, allowing grain growth to be studied (see Acke & van den Ancker [2004] for a review). Due to sensitivity limitations, *ISO* studies of silicates focused primarily on intermediate- or high-mass stars. Studies of TTs have therefore been limited, for the most part, to the $10 \mu\text{m}$ region. Although changes in the shape of the $10 \mu\text{m}$ emission features are observed in small samples of TTs (Przygodda et al. 2003; Kessler-Silacci et al. 2005), the cause of these changes is unclear and could be a combination of silicate grain growth and crystallization.

In this study, the improved sensitivity of the Infrared Spectrograph (IRS) aboard the *Spitzer Space Telescope* was used to expand such spectroscopic studies to include a large sample of disks around low-mass, Sun-like stars, creating a database analogous to *ISO* studies of high-/intermediate-mass stars. A few HAEBEs were also observed for comparison. The data presented here are part of the c2d *Spitzer* legacy program designed to study the evolution of circumstellar matter: From Molecular Cores to Planet-Forming Disks (Evans et al. 2003). This paper contains preliminary results from the program and focuses on statistical analysis of the strongest silicate features. It will be followed by a more detailed study of weaker features, including emission from crystalline silicates. The *Spitzer* IRS observations are described in § 2. In § 3 an inventory of the most prominent silicate emission features is presented. The observed spectra are compared with models of amorphous silicates in § 4. We perform a statistical analysis of the 10 and $20 \mu\text{m}$ silicate features and interpret these trends in terms of grain growth in § 5. Then, in § 6, we examine the relationship between the strength-shape trends found in § 5 and spectral type, stellar age, and $H\alpha$ equivalent width. Finally, in § 7, we discuss the crystalline silicate emission features in the observed spectra.

2. OBSERVATIONS

Spectra for 40 solar mass TTs and 7 intermediate-mass HAEBEs were obtained using the *Spitzer* IRS from 2003 December through 2004 December. The observations and source parameters are described in Table 1 for the TTs and HAEBEs in our sample. The spectra were observed with combinations of the short-low (SL), short-high (SH), long-low (LL), and/or long-

high (LH) modules (see Table 1, col. [4]). SL ($\lambda = 5.3\text{--}14.5 \mu\text{m}$) and LL ($\lambda = 14.2\text{--}40.0 \mu\text{m}$) spectra have a resolving power of $R = \lambda/\Delta\lambda \sim 100$, and the SH ($\lambda = 10.0\text{--}19.5 \mu\text{m}$) and LH ($\lambda = 19.3\text{--}37.0 \mu\text{m}$) spectra have a resolving power of ~ 600 . For approximately half of the sources, SL spectra are part of the GTO programs and not yet available for analysis, and therefore there is no spectral information shortward of $10.0 \mu\text{m}$. Exposure times were chosen to achieve signal-to-noise ratios of 50 and 100 for sources brighter and fainter than 500 mJy, respectively, with the weakest sources in our sample having fluxes of $\sim 100\text{--}200$ mJy at $15 \mu\text{m}$. All sources in the c2d program (Evans et al. 2003) that were observed prior to 2004 December and show evidence of silicate emission are included (47 sources; see Table 1).

Data reduction was done via the c2d Interactive Analysis (c2dia) reduction environment; c2dia contains optimized extraction algorithms developed by the c2d Legacy team.⁹ For wavelength calibration and IRS aperture definition, tools from the SMART software package (Higdon et al. 2004) were used.¹⁰ The extracted spectra were defringed using the IRSFRINGE package developed by the c2d team (Lahuis & Boogert 2003).¹¹ The spectra were extracted from the *Spitzer* Science Center (SSC) Basic Calibrated Data (BCD), pipeline version S11.0.2.¹² Two different extraction methods were used and compared to reduce spectral artifacts resulting from the extraction process.

The first method uses a full aperture extraction for SH and LH, and fixed-width aperture extraction for SL and LL. The extraction aperture was chosen to be large enough to enclose the complete source. (At the short-wavelength end, the extraction aperture is wider than that used in the SSC pipeline. However, since the SL and LL spectra are corrected for the background, as described below, this has a negligible effect on the extracted spectrum.) Bad pixels are corrected by interpolating in the cross-dispersion direction using a fit to the order-averaged source profile. For SL and LL the large apertures allow off-source spectra to be extracted, and these spectra were used to make wavelength-dependent background corrections. No background data were available for SH and LH spectra. A spectrum was extracted for each position, compared to check for artifacts, and finally averaged to produce the final spectrum.

In the second method, all BCDs from both dither positions are combined within the extraction algorithm. The extraction is performed by integrating over a source profile fit in the cross-dispersion direction. The source profile is a template created from standard-star observations (including sky measurements for SH and LH). The width and center of this template are adjusted for each observed source in our sample, to encompass 95% of the observed flux. This fitting process is performed for each source by using the highest quality data. Once the source profile is fit, a (uniform) local-sky background level, which is wavelength dependent, is estimated. This method also reduces the effects of unidentified bad pixels. In particular, in cases where the BCD images are largely affected by bad pixels (e.g., for LH), this method quite often gave significant improvements

⁹ The c2d extraction algorithms will become publicly available through the *Spitzer* Space Science Center as part of the c2d legacy program.

¹⁰ The SMART software package is publicly available at <http://ssc.spitzer.caltech.edu/archanaly/contributed/smart>.

¹¹ IRSFRINGE is included in SMART, but is also available as a stand-alone package from <http://ssc.spitzer.caltech.edu/archanaly/contributed/irsfringe/>.

¹² Recently, data from the SSC pipeline ver. S12, as well as more advanced versions of the extraction algorithms, have become available. We have verified that these do not have a significant impact on the reduced spectra and do not affect the results presented in this paper.

TABLE 1
SOURCE LIST

Source (1)	R.A. (J2000.0) (2)	Decl. (J2000.0) (3)	Observed Modules (4)	AOR Key (5)	Observation Date (6)	Age (Myr) (7)	H α EW ^a (Å) (8)	Spectral Type (9)	References (10)
RNO 15.....	03 27 47.68	+30 12 04.3	SL SH LH	0005633280	2004 Aug 30	...	116	...	1
Lk H α 327.....	03 33 30.41	+31 10 50.4	SL SH LH	0005634560	2004 Feb 3	1.4	51–65	K2	1, 2, 3
Lk H α 330.....	03 45 48.29	+32 24 11.8	SL SH LH LL1	0005634816	2004 Oct 25	...	11–20	G3	2, 3
IRAS 03446+3254 S.....	03 47 47.12	+33 04 03.4	SL SH LH LL1	0005635072	2004 Sep 29
V710 Tau ^b	04 31 57.79	+18 21 36.3	SH LH	0005636608	2004 Sep 29	0.7/0.4	11/89	M0.5/M3	4
Co Ku Tau 4.....	04 41 16.79	+28 40 00.5	SH LH	0005637888	2004 Sep 2	1.2–1.6	1.8–2.8	M1.5	2, 5, 6
IRAS 08267–3336.....	08 28 40.70	–33 46 22.3	SL SH LH LL1	0005639168	2004 Nov 11	...	25–35	K2–K3	7, 8
SX Cha.....	10 55 59.74	–77 24 39.9	SH LH	0005639424	2004 Aug 31	1–4	26.7	M0.5	9–11
SY Cha.....	10 56 30.47	–77 11 39.4	SH LH	0005639424	2004 Aug 31	2–5	24–64	M0	9–12
TW Cha.....	10 59 01.11	–77 22 40.8	SH LH	0005639680	2004 Sep 1	20	26.1	M0	9, 11
VW Cha ^b	11 08 00.53	–77 42 28.7	SH LH	0005639680	2004 Sep 1	0.4–0.9	72–147	K2	9–12
VZ Cha.....	11 09 23.80	–76 23 20.7	SH LH	0005640448	2004 Sep 2	4–10	58–71	K6	9–12
WX Cha ^b	11 09 58.75	–77 37 08.9	SH LH	0005640192	2004 Sep 1	1–5	65.5	K7–M0	9–11
ISO Cha 237.....	11 10 11.44	–76 35 29.2	SH LH	0005640448	2004 Sep 2	...	<3	M0	13
C7–11 ^b	11 10 38.01	–77 32 39.9	SH LH	0005640192	2004 Sep 1	0.2–1	4.0	K3	9, 14
HM 27.....	11 10 49.62	–77 17 51.7	SH LH	0005640192	2004 Sep 1	30–40	200.0	K7	9, 11
XX Cha.....	11 11 39.67	–76 20 15.1	SH LH	0005640448	2004 Sep 2	2–40	133.5	M2	9–11
T Cha.....	11 57 13.53	–79 21 31.5	SH LH	0005641216	2004 Jul 18	>12.5	2–10.0	G2–G8	15–17
IRAS 12535–7623.....	12 57 11.78	–76 40 11.5	SH LH	0011827456	2004 Aug 31	...	3.0	M0	17, 18
Sz 50.....	13 00 55.37	–77 10 22.2	SH LH	0011827456	2004 Mar 25	...	46	M3	19
HT Lup ^b	15 45 12.87	–34 17 30.6	SL SH LH	0009829120	2004 Aug 28	0.4–0.8	3–7	K2	11, 12, 20
GM Lup.....	15 46 44.68	–34 30 35.4	SL SH LH LL1	0005643520	2004 Aug 30	1.3–3.2	90–98	M2–M4	11, 20, 21
HW Lup.....	15 47 50.63	–35 28 35.4	SL LL1 LL2	0005643776	2004 Aug 30	1.2–2.7	115–155	M3	11, 20
Sz 73.....	15 47 56.98	–35 14 35.1	SL SH LH LL1	0005644032	2004 Aug 30	2.6–5.4	97–150	K2–M0	11, 20, 21
GQ Lup.....	15 49 12.10	–35 39 05.0	SL SH LH LL1	0005644032	2004 Aug 30	0.1–0.6	31–39	K7–M0	11, 12, 20
IM Lup.....	15 56 09.17	–37 56 06.4	SL SH LH LL1	0005644800	2004 Aug 30	0.1–0.6	4.7–8.1	M0	11, 12, 20
RU Lup.....	15 56 42.31	–37 49 15.5	SL SH LH LL1	0005644800	2004 Aug 30	0.1–0.5	136–216	K7–M0	11, 12, 20
RY Lup.....	15 59 28.39	–40 21 51.2	SL SH LH LL1	0005644544	2004 Aug 30	1.6–3.2	7.3	K0–K4	12, 20
EX Lup.....	16 03 05.52	–40 18 24.9	SL SH LH LL1	0005645056	2004 Aug 30	1.4–3.0	31–43	M0	11, 12, 20
Sz 102.....	16 08 29.70	–39 03 11.3	SL SH LH	0009407488	2004 Mar 25	...	377	K0–M4	20
AS 205 ^b	16 11 31.35	–18 38 26.1	SL SH LH	0005646080	2004 Aug 28	0.1	55–155	K5/M3	2, 3, 12, 22
VSSG1.....	16 26 18.86	–24 28 19.7	SH LH	0005647616	2004 Aug 28
Do Ar 24E ^b	16 26 23.38	–24 21 00.1	SH LH	0005647616	2003 Dec 15	1.5	5	K0	22, 23
GY 23.....	16 26 24.06	–24 24 48.1	SH LH	0005647616	2004 Aug 28	K5–M2	24
SR 21 N.....	16 27 10.28	–24 19 12.5	SH LH	0005647616	2003 Dec 15	1	0.54	G1–G2.5	22, 25
SR 9 ^b	16 27 40.27	–24 22 04.0	SH LH	0012027392	2004 Sep 2	...	6–14	K5–M2	2, 23, 24, 26
Haro 1-17.....	16 32 21.94	–24 42 14.7	SL SH LH LL1	0011827712	2004 Aug 29	...	15	M2.5	26
RNO 90.....	16 34 09.18	–15 48 16.8	SL SH LH LL1	0005650432	2004 Aug 28	6	76	G5	1
EC 82.....	18 29 56.89	+01 14 46.5	SL SH LH	0009407232	2004 Mar 27	...	5–11	M0	2, 27
CK 4.....	18 29 58.21	+01 15 21.7	SL SH LH	0009407232	2004 Mar 27
BF Ori.....	05 37 13.26	–06 35 00.6	SL SH LH LL1	0005638144	2004 Oct 3	2.0	6–11	A5–F6	2, 12, 28–30
RR Tau.....	05 39 30.52	+26 22 27.0	SL SH LH LL1	0005638400	2004 Sep 28	0.6	21.2–50	B8–A5	2, 28, 29, 31
HD 98922.....	11 22 31.67	–53 22 11.4	SH LH	0005640704	2004 Jan 4	...	27.9	B9	30, 31
DL Cha.....	13 06 08.36	–77 06 27.3	SH LH	0005642240	2004 Jul 14	M6	22
HD 135344.....	15 15 48.44	–37 09 16.0	SH LH	0005657088	2004 Aug 8	17	17.4	A0–F4	30, 32–34
HD 163296.....	17 56 21.29	–21 57 21.9	SH LH	0005650944	2004 Aug 28	4–6	12–17	A0–A2	15, 29–32
VV Ser.....	18 28 47.86	+00 08 39.8	SL SH LH	0005651200	2004 Sep 1	0.6	22–90	B1–A3	3, 28–31

NOTES.—Sources up to and including CK 4 are TTs; sources below CK 4 are HAEBEs. Units of right ascension are hours, minutes, and seconds, and units of declination are degrees, arcminutes, and arcseconds.

^a All H α lines are in emission, except that of SR 21, which is in absorption.

^b This source is a binary in 2MASS *K*-band images, with a separation <3'', and is unresolved with *Spitzer* IRS. *Spitzer* IRS observations are pointed at the center of the binary system. Stellar/disk parameters quoted from the literature include both sources.

REFERENCES.—(1) Levreault 1988; (2) Cohen & Kuhl 1979; (3) Fernandez et al. 1995; (4) Hartigan et al. 1994; (5) D'Alessio et al. 2005; (6) Kenyon et al. 1998; (7) Reipurth & Pettersson 1993; (8) Sahu & Sahu 1992; (9) Lawson et al. 1996; (10) Hartmann et al. 1998; (11) Appenzeller et al. 1983; (12) Reipurth et al. 1996; (13) Saffe et al. 2003; (14) Hartigan 1993; (15) van den Ancker et al. 1998; (16) Alcalá et al. 1995; (17) Gregorio-Hetem et al. 1992; (18) Sartori et al. 2003; (19) Hughes & Hartigan 1992; (20) Hughes et al. 1994; (21) Heyer & Graham 1989; (22) Prato et al. 2003; (23) Bouvier & Appenzeller 1992; (24) Luhman & Rieke 1999; (25) Martin et al. 1998; (26) Rydgren 1980; (27) Gomez de Castro 1997; (28) Natta et al. 1997; (29) Finkenzeller & Mundt 1984; (30) Acke et al. 2005; (31) The et al. 1994; (32) Thi et al. 2001; (33) Houk 1982; (34) Dunkin et al. 1997.

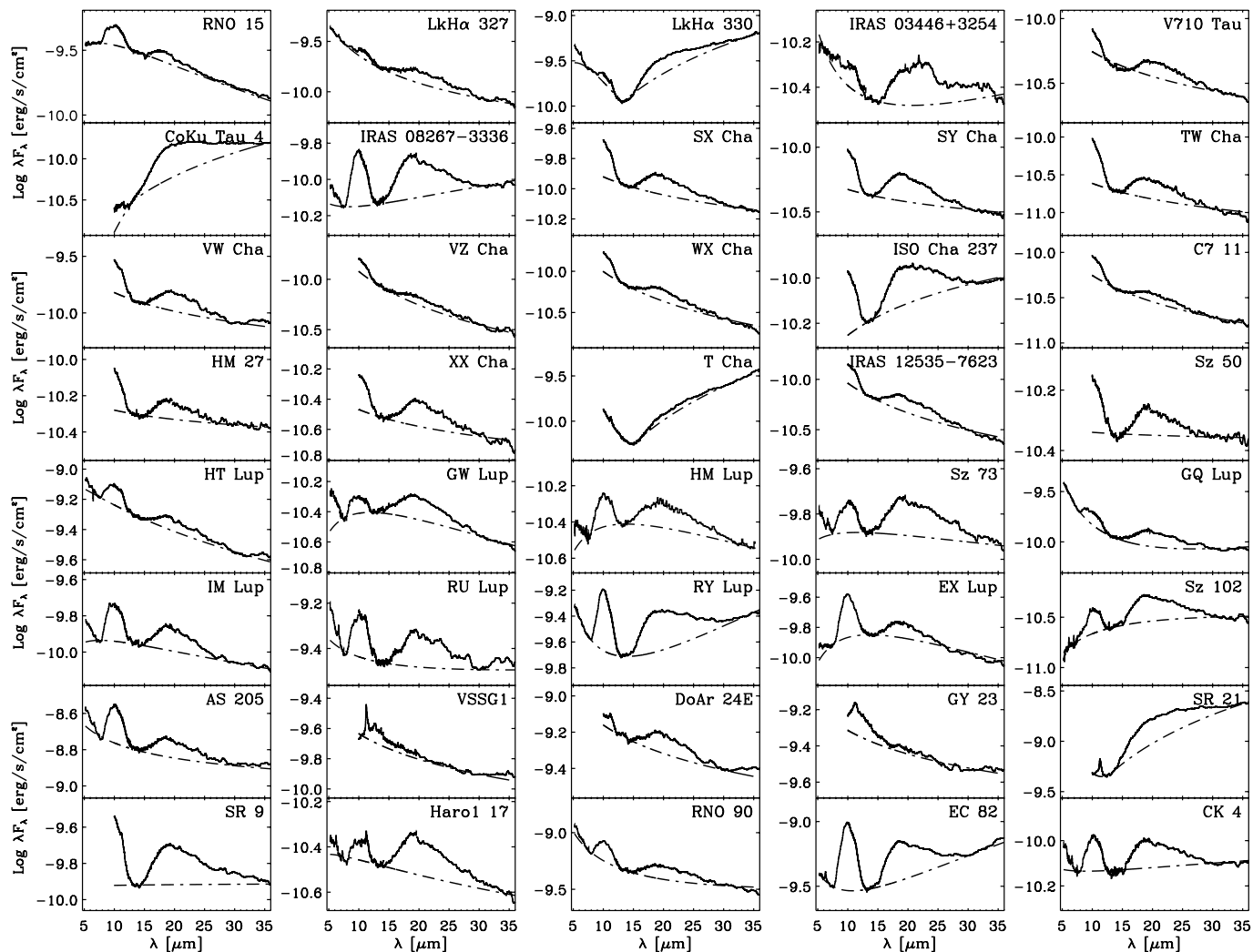


FIG. 1.—*Spitzer* mid- to far-IR spectra for TT disks. The spectra for each source are shown in units of $\log \lambda F_\lambda$. The SH and LH spectra have been median smoothed over three and five channels, respectively. No smoothing has been applied to the other modules. The dot-dashed line denotes the fit to the continuum described in the text and Table 2.

over the full aperture extraction. In the version of *c2dia* used here, the wavelength and flux calibration files produced by the SSC pipeline were used. For the S12 version of *c2dia*, the extraction algorithm is further developed and independently calibrated using a suite of standard-star calibrators. The extraction algorithms and the calibration involved will be described in more detail in F. Lahuis (2006, in preparation).

To correct for the possibly significant sky contribution in the SH and LH spectra, spectra obtained using full aperture extraction were corrected using the background estimate from the source profile-fitting extraction method. Both extractions were also compared with the spectra extracted from the SSC pipeline. In a few cases, particular modules suffered from artifacts due to data selection and/or bad-pixel correction, and the corresponding modules of the SSC spectrum were used. In cases where the SSC spectra were used, a correction to the zero level was applied to correct for background emission. Good sections of the background-corrected spectra were used to estimate the zero level in the other modules. When necessary, individual orders and/or modules were multiplied by small ($<5\%$ and $<15\%$, respectively) constant factors to correct flux offsets between orders/modules. These flux offsets are likely related to pointing errors resulting in the source

not being centered in the aperture and seem to be corrected in the SSC pipeline version S12.

3. INVENTORY OF SILICATE EMISSION FEATURES

The extracted spectra of TT and HAEBE disks are shown in Figures 1 and 2, respectively. Two sources, HT Lup and HD 163296, were observed twice, once in IRS staring mode and once in spectral mapping mode. The two observations for each source do not differ significantly; integrated intensities, peak-to-continuum fluxes, and feature widths agree to within $\sim 7\%$ for the 10 and 20 μm features. Therefore, only one spectrum for each source is included in Figures 1 and 2 and Table 2.

An inventory of the silicate emission features is presented in Table 2. The features listed are relatively isolated and can be clearly identified in the spectra. The peak wavelengths of the silicate features depend on the exact composition and grain size of the dust. Therefore, the broad amorphous silicate features, corresponding to the Si–O stretching and O–Si–O bending modes, are labeled as ~ 10 and ~ 20 μm . The peaks of the identified crystalline silicate features may vary within the wavelength ranges given in Table 2, which correspond to the ranges in peak wavelengths for features of crystalline enstatite and forsterite of

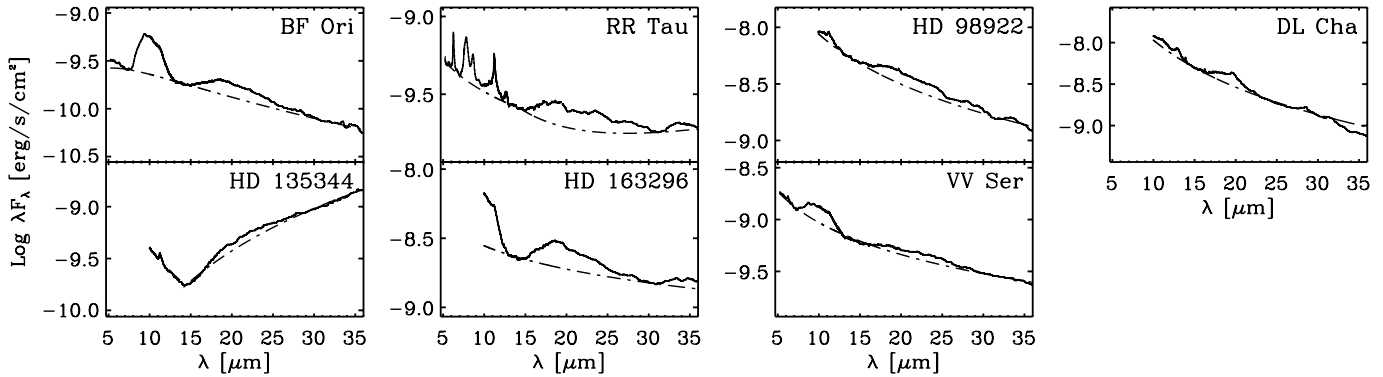


FIG. 2.—*Spitzer* mid- to far-IR spectra for HAEBE disks. The spectra for each source are shown in units of $\log \lambda F_\lambda$. The SH and LH spectra have been median smoothed over three and five channels, respectively. No smoothing has been applied to the other modules. The dot-dashed line denotes the fit to the continuum described in the text and Table 2.

sizes between 1 and 10 μm . Features are marked with Y, T, or N if the feature is detected, tentatively detected, or absent.

Emission at 10 and 20 μm from amorphous silicates dominates the spectra of most of the disks observed. Broad 20 μm amorphous silicate features can be seen in almost all of the spectra, while the 10 μm amorphous silicate features are slightly less prominent (seen in 42 of 47 spectra). Emission near 11.3 μm , due to PAH or crystalline forsterite, is clearly identified in $\sim 1/3$ of the spectra. This is a lower limit, however, as tentative emission is seen in several additional spectra in which the presence of artifacts prevent further analysis. *ISO* observations of disks around HAEBEs (Acke & van den Ancker 2004) report 11.3 μm emission from $\sim 1/4$ of the observed sources, but the same studies find that the fraction showing PAH emission at 7.7 μm is much higher (57%).

The lattice modes of crystalline silicates at $\lambda > 25 \mu\text{m}$ appear to be more prominent than the 11.3 μm feature in our data and do not suffer from confusion with PAH emission. Approximately half of the disks in our sample show emission features near 28 μm and in the 33–35 μm region, characteristic of crystalline enstatite and forsterite. The 24–36 μm region is shown for six of these sources in Figure 3, with shaded regions depicting the typical positions of enstatite and forsterite features. These data indicate that crystalline silicates can be quite prominent in TT disks. This is in surprising contrast to ground-based studies of silicates in the 10 μm region, which found crystalline silicate emission from very few TTs (see Kessler-Silacci et al. [2005] for a summary).

As the 10 and 20 μm emission features from amorphous silicates are the most easily identified and isolated, the rest of this paper focuses on the analysis of these features. PAHs will be discussed in detail in V. Geers et al. (2006, in preparation), and SEDs will be modeled in J.-C. Augereau et al. (2006, in preparation). Silicate composition will be modeled in more detail by J. Kessler-Silacci et al. (2006, in preparation), including analysis of all crystalline silicate features.

4. COMPARISONS WITH MODELS OF AMORPHOUS SILICATES

As mentioned above, the peak wavelengths, strengths, and shapes of the silicate features depend on the exact composition, sizes, and shapes of the silicates. Therefore, in order to interpret the observed silicate emission, we must compare our data with models of the emission from a variety of silicate grains. Modeled grain opacities can be compared to the observed emission once

the continuum is removed. In § 4.1 we describe the method of continuum normalization used here. Our procedure for modeling of grain opacities from laboratory optical constants is described in § 4.2. Finally, in § 4.3, we quantitatively compare modeled and observed opacities in the 10 and 20 μm regions.

4.1. Continuum Normalization

Continuum normalization was performed using one of three methods, as noted in Table 2, and is described as follows.

1. For spectra that include SL (e.g., RNO 15), a second-order polynomial was fit to the continuum in the following regions: 6.8–7.5, 12.5–13.5, and 30–36 μm .

2. For spectra that do not include SL (e.g., V710 Tau), the continuum was obtained with a linear fit to the 12.5–13.5 and 30–36 μm regions.

3. In cases where the SED appears to fall sharply with increasing wavelength shortward of 12–15 μm and then rises sharply beyond $\sim 15 \mu\text{m}$ (e.g., Lk H α 330), we fit the 10 and 20 μm features separately, using a second-order polynomial fit for wavelengths shortward of $\sim 15 \mu\text{m}$ and a linear fit longward of $\sim 15 \mu\text{m}$. These sources will be discussed in more detail in J. Brown et al. (2006, in preparation).

The continuum fits are overlaid on the observed spectra in Figures 1 and 2 as dot-dashed lines. The continuum-fitting regions were chosen to represent the areas least affected by features in the spectra and, as shown, vary slightly from source to source. Opacities obtained from laboratory spectra of amorphous olivines (see § 4) indicate that the regions chosen above should be clear of amorphous silicate emission features, with the exception of the region from ~ 13 –15 μm , which likely contains contributions from the wings of both the 10 and 20 μm features. Thus, the feature strengths obtained from the continuum-normalized spectra will be underestimated.

After the continuum fitting was performed, the normalized spectra S_ν were obtained via application of the formula,

$$S_\nu = 1 + \frac{(F_\nu - F_{\nu,c})}{\langle F_{\nu,c} \rangle},$$

where F_ν is the observed spectrum and $F_{\nu,c}$ is the fitted continuum, both in units of janskys, and $\langle F_{\nu,c} \rangle$ is the frequency-averaged continuum flux. We divide by a frequency-averaged value of the continuum flux in order to remove any dependence

TABLE 2
SILICATE EMISSION FEATURES

Species λ (μm) (1)	Silicates ^a (~10) (2)	PAH / Cr. Sil. ^b (11.2–11.3) (3)	Silicates ^a (~20) (4)	Cr. Sil. ^c (28–29) (5)	Cr. Sil. ^d (33–35) (6)	Normalization Method ^e (7)
RNO 15.....	Y	T	T	Y	T	1
Lk H α 327.....	Y	Y	Y	Y	Y	1
Lk H α 330.....	Y	Y	Y	T	N	3
IRAS 03446+3254.....	Y	Y	Y	N	T	1
V710 Tau.....	Y	T	Y	T	T	2
Co Ku Tau 4.....	Y	T	Y	N	N	2
IRAS 08267–3336.....	Y	N	Y	N	N	1
SX Cha.....	Y	T	Y	T	Y	2
SY Cha.....	Y	T	Y	T	T	2
TW Cha.....	Y	T	Y	T	T	2
VW Cha.....	Y	T	Y	Y	Y	2
VZ Cha.....	Y	T	T	Y	Y	2
WX Cha.....	Y	T	Y	T	Y	2
ISO Cha 237.....	Y	T	Y	T	T	2
C7–11.....	Y	T	Y	T	T	1
HM 27.....	Y	N	Y	T	T	2
XX Cha.....	Y	N	Y	T	T	2
T Cha.....	N	Y	T	N	N	3
IRAS 12535–7623.....	Y	T	Y	Y	N	2
Sz 50.....	Y	N	Y	N	T	2
HT Lup.....	Y	T	Y	T	Y	1
GW Lup.....	Y	T	Y	T	T	1
HM Lup.....	Y	T	T	T	T	1
Sz 73.....	Y	T	Y	T	T	1
GQ Lup.....	Y	T	Y	Y	Y	1
IM Lup.....	Y	T	Y	T	T	1
RU Lup.....	Y	T	Y	Y	Y	2
RY Lup.....	Y	N	Y	N	N	1
EX Lup.....	Y	T	Y	T	T	1
Sz 102.....	Y	T	Y	N	Y	1
AS 205.....	Y	T	Y	T	T	1
VSSG1.....	Y	Y	N	Y	T	2
Do Ar 24E.....	Y	Y	Y	Y	T	2
GY 23.....	N	Y	N	Y	T	2
SR 21.....	N	Y	Y	T	T	3
SR 9.....	Y	T	Y	T	N	2
Haro 1-17.....	Y	Y	Y	Y	Y	1
RNO 90.....	Y	N	Y	T	N	1
EC 82.....	Y	N	Y	N	T	1
CK 4.....	Y	T	Y	T	Y	1
BF Ori.....	Y	T	Y	T	Y	1
RR Tau.....	N	Y	Y	Y	Y	1
HD 98922.....	T	Y	Y	Y	Y	2
DL Cha.....	T	Y	Y	Y	N	2
HD 135344.....	N	Y	T	N	N	3
HD 163296.....	Y	T	Y	T	Y	2
VV Ser.....	Y	T	Y	T	Y	1

NOTES.—Sources up to and including CK 4 are TTs; sources below CK 4 are HAEBEs. Features are marked with a Y if detected, N if not detected, or T if the identification is tentative.

^a Broad, primarily amorphous olivine/pyroxene emission features.

^b Feature includes PAH at 11.2 μm and crystalline forsterite at 11.3 μm (V. Geers et al. 2006, in preparation).

^c Feature includes crystalline forsterite near 27.9 μm and/or crystalline enstatite near 28.5 μm .

^d Feature includes crystalline forsterite near 33.6 μm and/or crystalline enstatite near 34.5 μm .

^e Continuum-normalization procedure, as described in the text.

on the slope of the continuum. This normalization method, including the offset of 1.0, is consistent with the method used by van Boekel et al. (2003) and Przygodda et al. (2003), to which we compare it in § 5. As the continuum may change dramatically between 10 and 20 μm for some sources (e.g., Co Ku Tau 4), $\langle F_{\nu,c} \rangle$ is calculated separately for regions of $\lambda = 5\text{--}13$ μm and $\lambda = 13\text{--}37$ μm . If $F_{\nu,c}$ is used in place of $\langle F_{\nu,c} \rangle$, then the nor-

malization would reduce to $F_{\nu}/F_{\nu,c}$, which is approximately equal to the optical depth for optically thin emission,

$$\frac{F_{\nu}}{F_{\nu,c}} = 1 - e^{-\tau_{\nu}} \approx \tau_{\nu} (\tau_{\nu} \ll 1),$$

where τ_{ν} is the optical depth as a function of frequency.

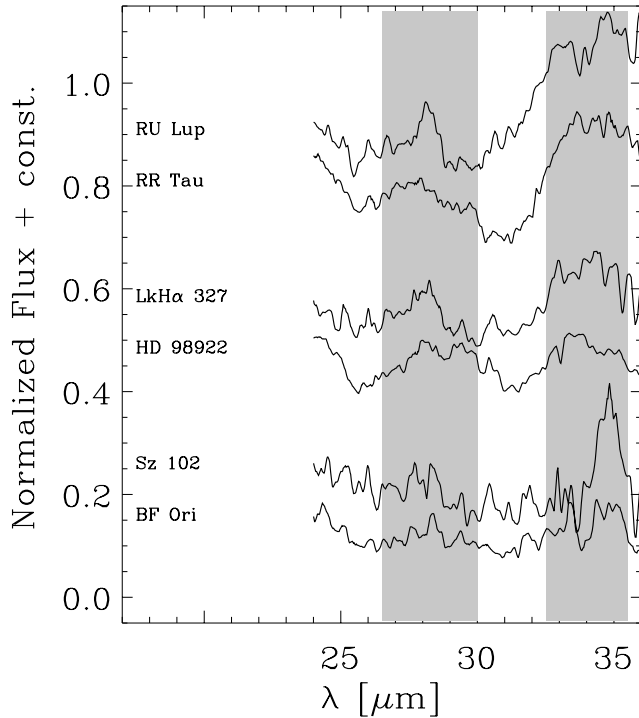


FIG. 3.—Continuum-normalized and smoothed LH spectra for six of the sources that show emission from crystalline silicates in the 26.5–30 and/or 33–35 μm regions (shaded). Each pair of spectra contains one HAEBE (bottom) and one TT (top). Features in the 26.5–30 μm region tend to be narrower for the TTs.

Comparison between the two continuum normalization methods for the spectra in the c2d sample shows that the 10 and 20 μm feature strengths and shapes do not differ significantly ($\sim 5\%$ and $\sim 10\%$, respectively).

Although continuum normalization has been previously used to interpret ground-based and *ISO* observations of 10 μm silicate emission features (Honda et al. 2003; van Boekel et al. 2003; Przygodda et al. 2003; Acke & van den Ancker 2004), it was previously not applied to 20 μm silicate features because the emission feature strength can be confused by a rising continuum. To address this issue, we plot the spectral index (α) of the derived continuum from 13 to 35 μm versus the strength of the continuum normalized 20 μm feature ($S_{\text{peak}}^{20\mu\text{m}}$) in Figure 4. The spectral indices are calculated as

$$\alpha_{a-b} = -\frac{\log(\lambda_b F_{\lambda_b}) - \log(\lambda_a F_{\lambda_a})}{\log(\lambda_b) - \log(\lambda_a)},$$

where $\lambda_a = 13 \mu\text{m}$, $\lambda_b = 35 \mu\text{m}$, and F_{λ_x} is the flux density at wavelength λ_x in units of $\text{ergs cm}^{-2} \text{s}^{-1} \mu\text{m}^{-1}$. The bulk of the spectra are relatively flat or falling in units of λF_{λ} , with $\alpha = 0-1$ and $S_{\text{peak}}^{20\mu\text{m}} = 1.1-1.5$ (see Fig. 4). The five sources for which we use continuum-fitting method 3 have spectra that are steeply rising from 13 to 35 μm ($\alpha = -1$ to -2) and lie along the bottom of Figure 4. A few other sources with rising spectra (e.g., RY Lup, [EC92] 82, hereafter EC 82) can be seen on the right-hand side of Figure 4. We find that the spectral index and the derived strength of the 20 μm feature is at most weakly correlated (at the 80% significance level), with the more steeply rising spectra corresponding to the stronger 20 μm silicate features. There is thus a small chance that the shape/strength parameters derived for a particular source may be related to the continuum fit. As stated above,

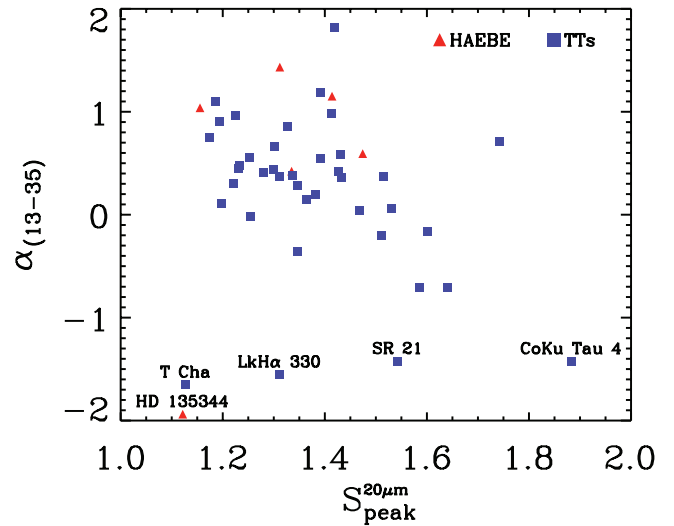


FIG. 4.—Evaluation of the continuum normalization method at 20 μm . Spectral indices in the range 13–35 μm are plotted vs. the strengths of the continuum-normalized 20 μm silicate emission features for all sources. TTs are denoted by squares, and HAEBEs are denoted by triangles. The mid-IR spectral indices and 20 μm feature strengths appear to be, at most, weakly inversely correlated ($r = -0.2$, 80% significance), with more steeply rising spectra corresponding to stronger 20 μm silicate emission features.

modeling of individual spectra without continuum normalization will be presented in J. Kessler-Silacci et al. (2006, in preparation).

A representative sample of continuum-normalized spectra in the 10 and 20 μm regions is shown in Figures 5a and 5b. A large fraction of the observed spectra is similar to GQ Lup, possessing weak and sometimes flat-topped 10 μm silicate emission features. A few others possess centrally peaked 10 μm features, with large peak-to-continuum flux, as is the case for EC 82. The rest of the sample falls between these two extremes. Most spectra show 20 μm features with lower peak-to-continuum flux in the 20 μm region with respect to that at 10 μm .

4.2. Modeling Dust Optical Properties

To aid in the interpretation of the observed silicate emission features, we model the opacities for a sample of grains of different shape, size, and composition. Optical constants are obtained from laboratory data available from the Jena–St. Petersburg database¹³ (see Table 3; Henning et al. 1999). Absorption efficiencies (Q_{abs}) are then calculated for spherical, homogeneous grains of different sizes, representing compact grains, using Mie theory (Mie 1908). Interstellar dust, however, is not likely to be spherical, and images of interplanetary dust particles (see Bradley [2003] for a review) suggest that nebular dust likely consists of porous and irregularly shaped aggregates. In addition, the positions of the features in the mass absorption coefficients of crystalline silicates derived via Mie theory do not agree with observations of astronomical silicates (e.g., Bouwman et al. 2001). Therefore, to simulate porous or irregularly shaped particles, we calculate opacities for continuous distributions of hollow spheres (DHS), using the statistical method described in Min et al. (2005). In the Mie method, the particle can be represented by a homogeneous, filled sphere. In the DHS method, a distribution of hollow spherical silicate shells is used such that the vacuum volume filling fractions vary, but the masses remain the same as that of the homogeneous, filled sphere. The DHS method averages the scattering and absorption/emission

¹³ See <http://www.astro.uni-jena.de/Laboratory/Database/databases.html>.

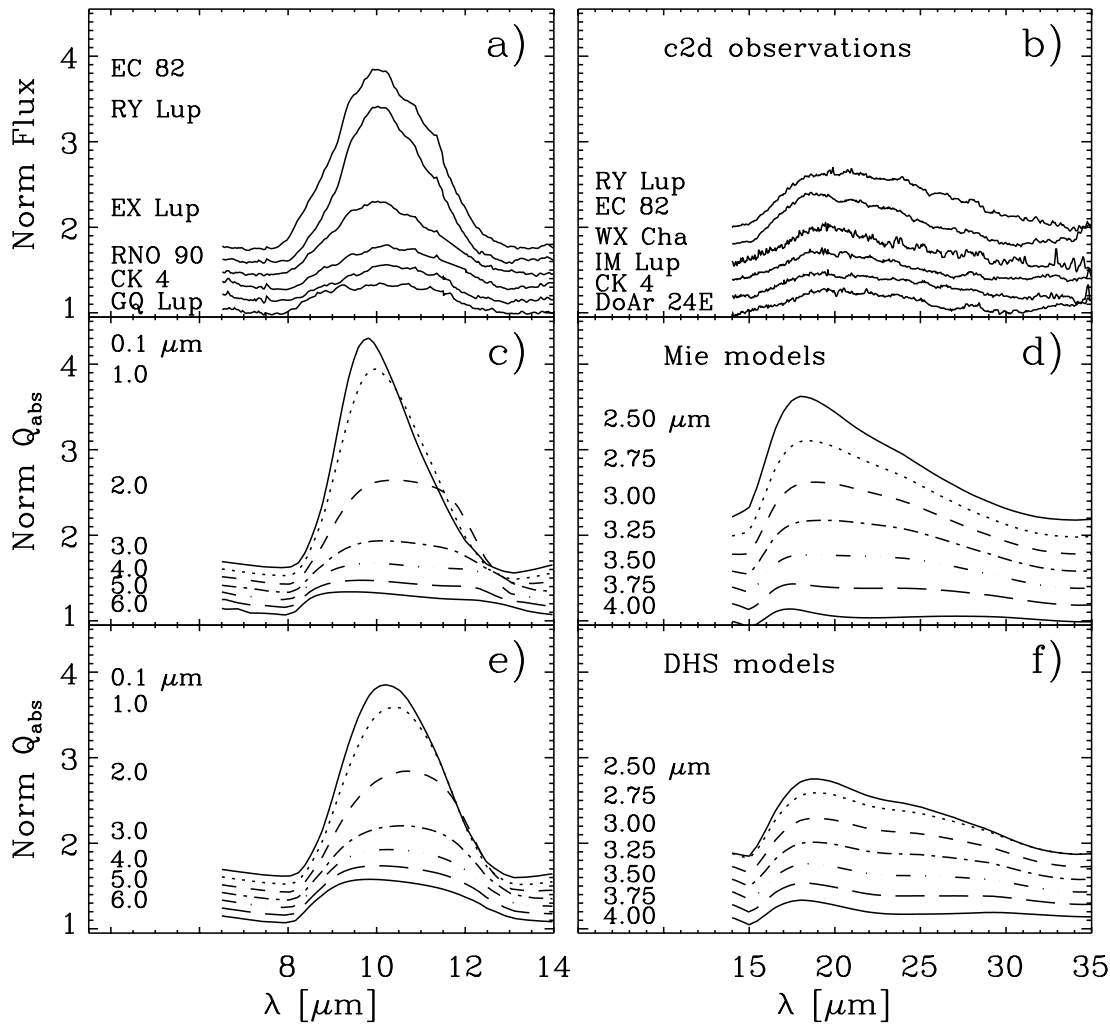


FIG. 5.—Evidence of grain growth in the Si—O stretching and O—Si—O bending mode features. The top panels show the observed normalized spectra in the (a) 10 μm and (b) 20 μm regions for subsamples of our sources. The bottom two panels show the normalized absorption efficiencies (Q_{abs}) for models of spherical grains of amorphous olivines with various grain sizes calculated for the 10 and 20 μm regions. Models of filled homogeneous spheres calculated using Mie theory are shown in (c) and (d), and models of hollow spheres calculated using DHS theory are shown in (e) and (f). Spectra in all panels have been artificially shifted along the y -axis by a constant value as a function of wavelength, such that the spectrum of each source could be seen more clearly. The minimum of each normalized spectra was 1.0 prior to adding these constants.

cross sections of the set of hollow spheres, and these cross sections can be compared to those of the homogeneous filled sphere of the same mass. The optical properties of individual large hollow spheres are calculated using the algorithm proposed by Toon & Ackerman (1981) for coated spheres, which was found to be extremely accurate (to four decimal places) when compared to measured efficiencies. We apply a simple analytical application of the Rayleigh approximation as described in Min et al. (2003) for small grains with $x = 2\pi a/\lambda \ll 1$ and $|m| \ll 1$, where a is the radius of the particle and m is the refractive index.

TABLE 3
LIST OF ADOPTED GRAIN MATERIAL

Dust Type	Formula/Name	References
Amorphous olivine	MgSiO_4	Dorschner et al. (1995)
Amorphous pyroxene.....	$\text{Mg}_{0.5}\text{Fe}_{0.5}\text{SiO}_3$	Dorschner et al. (1995)
Crystalline forsterite.....	Mg_2SiO_4	Servoin & Piriou (1973)
Crystalline enstatite.....	MgSiO_3	Jäger et al. (1998)
Amorphous carbon.....	ACAR	Zubko et al. (1996)

Figures 6–8 show the absorption efficiencies (Q_{abs}) for grains of amorphous olivine, pyroxene, and crystalline forsterite for a range of sizes between 0.1 and 10 μm . Here we have used the grain radius (a) of the filled, homogeneous sphere as a proxy for the grain mass, which is held constant for both Mie and DHS models. As indicated in Figure 6, the slope of the overall spectrum varies significantly as a function of grain size. Thus, in order to compare the model Q_{abs} to the normalized *Spitzer* spectra, we use a “continuum” fitting method that is similar to that applied to the *Spitzer* spectra. Although this method will most likely not find the physical continuum level, treating the observed and modeled spectra in the same manner will enable a more robust comparison. Normalized Q_{abs} in the 10 and 20 μm regions for the modeled grain opacities of amorphous olivines calculated using Mie and DHS are shown in Figures 5c–5f, respectively. The comparison of these normalized absorption efficiencies to the observed spectra involves an implicit assumption about the dominance of silicate emission in the 8–35 μm region. Disk models (e.g., Pollack et al. 1994) based on solar elemental abundances find that the main refractory components are olivine, pyroxene, carbonaceous material and/or organics, water ice, troilite (FeS),

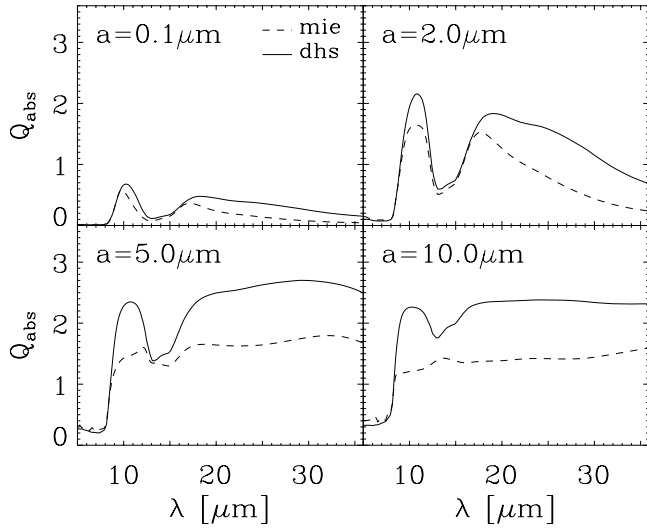


FIG. 6.—Absorption efficiencies for amorphous olivine for grain sizes of 0.1, 2, 5, and 10 μm . In the top left panel, Q_{abs} for $a = 0.1 \mu\text{m}$ has been multiplied by a factor of 5. The dashed lines show Q_{abs} calculated using Mie theory for spherical grains. The solid lines show Q_{abs} calculated using the DHS method described in the text.

and metallic iron. They find that silicates clearly dominate the opacity for $T > 500 \text{ K}$, but at lower temperatures the shapes and strengths of the 10 and 20 μm features can be affected by the opacities of organics and water ice. The silicate emission studied here arises from the warm surface layers of these disks, and ices are unlikely to play any role. In addition, the excellent correspondence between the modeled silicate opacities and the observed spectra (see Fig. 5), in both contrast and spectral shape, suggests that we are in a regime in which this comparison is valid.

4.3. Grain Growth

Both the shape and strength of the silicate features are dependent on grain size, with Mie and DHS models possessing slightly different silicate features. Here we compare the 10 and

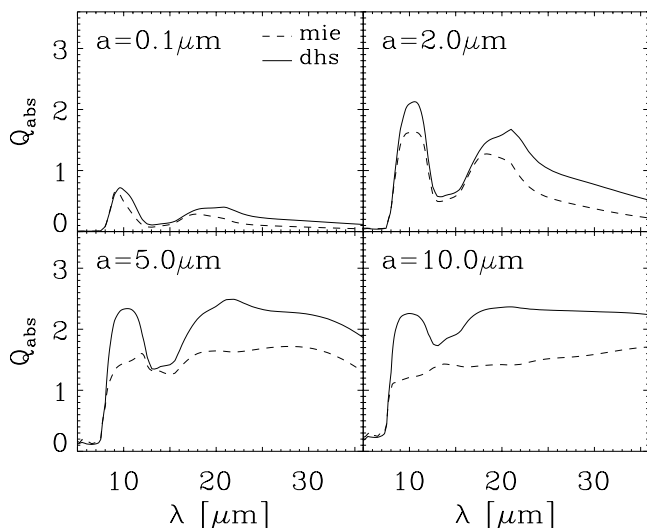


FIG. 7.—Absorption efficiencies for amorphous pyroxene for grain sizes of 0.1, 2, 5, and 10 μm . In the top left panel, Q_{abs} for $a = 0.1 \mu\text{m}$ has been multiplied by a factor of 5. Lines are as in Fig. 6.

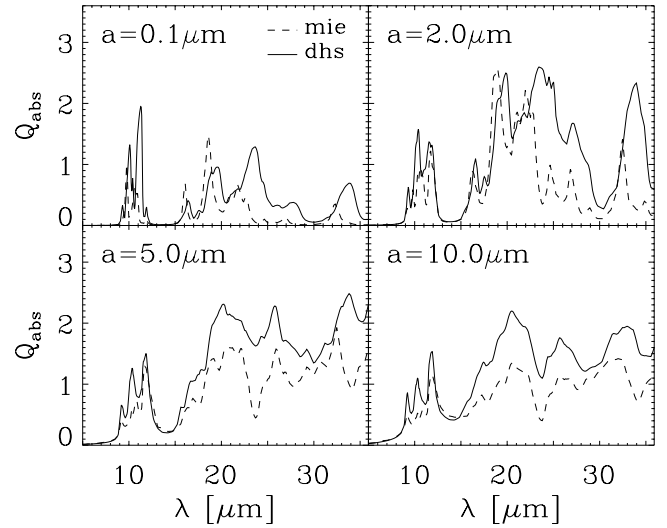


FIG. 8.—Absorption efficiencies for crystalline forsterite for grain sizes of 0.1, 2, 5, and 10 μm . In the top left panel, Q_{abs} for $a = 0.1 \mu\text{m}$ has been multiplied by a factor of 5. Lines are as in Fig. 6. Note that the results of Mie/DHS theory for large ($a > 2 \mu\text{m}$) forsterite grains have not been confirmed by laboratory studies. In addition, emission feature positions are offset for Mie and DHS models. DHS models have been found to more closely agree with astronomical observations of silicates in disks (van Boekel et al. 2005).

20 μm silicate features in the observed spectra to the Mie and DHS models (Fig. 5).

Both Mie and DHS models show that the 10 μm silicate feature strength decreases, and the feature flattens, as a function of grain size. The 10 μm feature strength for Mie models (Fig. 5c) is largest for grain sizes of $a \approx 0.1 \mu\text{m}$. When $a = 8 \mu\text{m}$, the feature has almost disappeared. A similar trend can be seen in the models of hollow spheres using DHS methods in Figure 5e. The shape of the 10 μm feature is slightly more round for the DHS than Mie models, however, and the peak strength is underestimated (with respect to Mie models) for smaller grain sizes ($a = 0.1 \mu\text{m}$) and overestimated for larger grain sizes ($a = 6.0 \mu\text{m}$).

For the 20 μm feature (Figs. 5d and 5f), again we see that for both Mie and DHS models, the feature strength decreases and broadens when the grain size is increased from 2.5 to 5.0 μm . The emission feature also appears to shift to longer wavelength with increasing grain size, peaking near 18 μm (similar to our observations) for Mie and DHS models of amorphous olivines with grain sizes of $a = 3\text{--}5 \mu\text{m}$. The shapes of the 20 μm features of the Mie and DHS models are also slightly different, with DHS models showing a much flatter feature. In addition, the peak strengths of the DHS models are smaller than those of the Mie models for smaller grain sizes ($a = 2.5 \mu\text{m}$) and larger than the Mie models for larger grain sizes ($a = 4.0 \mu\text{m}$).

The observed spectra (Figs. 5a and 5b) are quite similar to the models, differing slightly for the weakest emission features. The weakest 10 μm features observed toward several sources are similar to the models of 5 μm amorphous olivine grains, but appear to be slightly narrower and more sharply peaked at the edges of the feature. Additional emission from crystalline silicates may be necessary to reproduce the “boxy” structure of such features. The strongest observed 20 μm features are similar in strength to models of amorphous olivine with grain sizes $> 2 \mu\text{m}$. The weakest features are similar in strength to models of amorphous olivine with sizes less than approximately 4.5 μm .

Thus, the comparison of the observed spectra with modeled amorphous olivine opacities provides a qualitative understanding

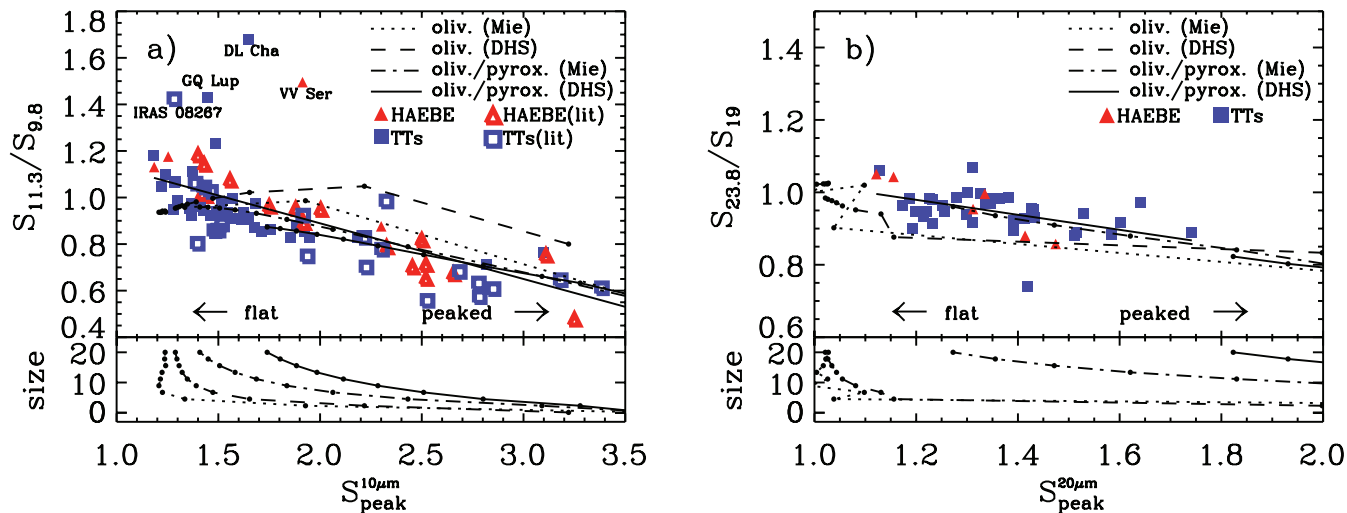


FIG. 9.—Shape and strength of the (a) $10\ \mu\text{m}$ and (b) $20\ \mu\text{m}$ silicate features. The shapes of the features (probed by the normalized flux ratios, $S_{11.3}/S_{9.8}$ and $S_{23.8}/S_{19}$) are plotted vs. the feature strengths ($S_{\text{peak}}^{10\ \mu\text{m}}$ and $S_{\text{peak}}^{20\ \mu\text{m}}$) in the top panels of each figure. The data observed in this study are denoted by filled squares (TTs) and filled triangles (HAEBEs). Data for $10\ \mu\text{m}$ silicate features from the literature (van Boekel et al. 2003; Przygodda et al. 2003; Kessler-Silacci et al. 2005) are represented by open symbols. The black line in (a) indicates the correlation found for the $10\ \mu\text{m}$ features including all data, and follows the relation $y = A + Bx$, where $A = 1.37 \pm 0.05$ and $B = -0.24 \pm 0.03$, with a correlation coefficient of $r = -0.7$. The $20\ \mu\text{m}$ features also show a correlation ($r = -0.5$), with $A = 1.23 \pm 0.08$ and $B = -0.21 \pm 0.06$. Models of amorphous olivines, pyroxenes, and mixtures of the two for various grain shapes are overlaid as dot-dashed lines connecting points representing grains with a linear size distribution between 0.1 and $20\ \mu\text{m}$ (see text for details). The bottom panels of each figure show the grain size vs. peak strength for the models.

of the effect of grain growth on the 10 and $20\ \mu\text{m}$ features observed for our sample. In § 5, we perform a more quantitative analysis.

5. STATISTICAL ANALYSIS OF THE 10 AND $20\ \mu\text{m}$ FEATURES

Previous observations of disks around HAEBEs and TTs have shown that plots of the shape versus strength of the $10\ \mu\text{m}$ emission feature may be indicative of grain growth. In § 5.1 we interpret variations in the shape and strength of the observed silicate features in terms of source-to-source variations in grain size. Because it is important to understand the uniqueness of this interpretation, in § 5.2 we evaluate the dependence of the 10 and $20\ \mu\text{m}$ feature strengths on several other grain properties, including the grain size distribution, relative sizes of grains emitting at 10 and $20\ \mu\text{m}$, grain composition, crystallinity, and porosity.

5.1. Strength-Shape Trends

We find that the shapes of the continuum-normalized $10\ \mu\text{m}$ emission feature from HAEBEs and TTs are proportional to the feature strengths (as was previously noted by van Boekel et al. [2003] and later Przygodda et al. [2003] and Kessler-Silacci et al. [2005]). In Figure 9a, we plot the shape of the $10\ \mu\text{m}$ feature versus the feature strength, $S_{\text{peak}}^{10\ \mu\text{m}}$. As a proxy for the feature shape, we use the ratio of the normalized flux at the peak of the crystalline silicate feature relative to that of the amorphous silicate feature ($S_{11.3}/S_{9.8}$). The fluxes are integrated over regions of $\pm 0.1\ \mu\text{m}$ around the central wavelength. Data from the literature (“lit,” Fig. 9a, open symbols; van Boekel et al. 2003; Przygodda et al. 2003; Kessler-Silacci et al. 2005) are plotted, in addition to the data collected in this study (“c2d,” Fig. 9a, filled symbols). Source parameters and original references for the lit sample are listed in Table 4. There are five sources that overlap between the c2d and lit samples: RU Lup, AS 205, Do Ar 24E, HD 98922, and HD 163296. The $10\ \mu\text{m}$ feature strengths and shapes of these sources are consistent to within $11\% \pm 7\%$. In the statistical analysis, we use only our data for the duplicate sources, except in the case of AS 205, for which we use the Przygodda

et al. (2003) spectra for each source in the binary. There is a strong correlation for the entire sample of $10\ \mu\text{m}$ features, which is consistent with that first noted by van Boekel et al. (2003). This trend is similar to changes in silicate emission due to grain size variations illustrated in Figure 5, with flatter, weaker $10\ \mu\text{m}$ emission features, characteristic of larger grain sizes, appearing in the upper left region of Figure 9a.

In order to interpret this trend more quantitatively, we perform the same analysis for the continuum-normalized model opacities discussed in § 4.2. We include grains of amorphous olivine, pyroxene, and mixtures of the two for grain sizes between 0.1 and $20\ \mu\text{m}$. The Maxwell Garnett mixing rule (Maxwell Garnett 1904) is used to calculate effective cross sections for all mixtures. The model data are overlaid on the observational data in Figure 9a, with lines connecting points of varying grain size for each model. Note that the peak strength corresponds to different sizes, depending on the dust composition and whether DHS or Mie models are used (see Fig. 9a, bottom).

The observed trend is best fit with models of amorphous olivine-pyroxene mixtures. Models of pure amorphous olivines calculated using DHS are inconsistent with the observations. These models possess generally larger $S_{11.3}/S_{9.8}$ ratios than the data, particularly for strong features. Mie models of pure amorphous olivines fit the data much better, but begin to deviate from observations near $S_{\text{peak}}^{10\ \mu\text{m}} \approx 2$. The slope of the observed trend can be best matched using mixtures with 30% amorphous olivines and 70% amorphous pyroxenes. This pyroxene fraction is much larger than that inferred for diffuse ISM grains in the Galactic center (15.1% pyroxene; Kemper et al. 2004), indicating a substantial conversion of olivines to pyroxenes in young stellar environments. Enhanced pyroxene-to-olivine abundances were previously observed toward high-mass protostars with *ISO* and may be explained by He^+ sputtering in high-velocity shocks (Demyk et al. 2001 and references therein).

Models of olivine-pyroxene mixtures fit the data best for homogeneous filled spheres (Mie) and hollow spheres (DHS), but do not fit equally well for all grain sizes (peak strengths). For the weakest $10\ \mu\text{m}$ features ($S_{\text{peak}}^{10\ \mu\text{m}} \leq 1.75$), hollow sphere

TABLE 4
STELLAR/DISK PARAMETERS FOR MIR SPECTRA FROM THE LITERATURE

Source	R.A. (J2000.0) ^a	Decl. (J2000.0) ^a	Spectroscopy Reference ^b	Age (Myr)	H α EW ^c (Å)	Spectral Type	References
GG Tau ^d	04 32 30.31	+17 31 41.0	Prz	1.7	31–54	K6–K7	1, 2, 3
AA Tau	04 34 55.45	+24 28 53.7	K-S	0.9–2.4	37.1	K7	1, 2, 4, 5
Lk α 15	04 39 17.80	+22 21 04.5	K-S	2–11	23.1	K5	1, 4, 6
DR Tau	04 47 05.48	+16 58 42.1	Prz	3.8	95.4	K4	1, 2
GM Aur	04 55 10.90	+30 22 01.0	K-S	0.9–1.8	96.5	K7	1, 2, 4
SU Aur	04 55 59.38	+30 34 01.5	Prz	3.0	3.5	G2	2, 7
GW Ori	05 29 08.39	+11 52 12.7	Prz	...	27–29	G5	2, 3
CR Cha	10 59 06.97	–77 01 40.3	Prz	...	30–44	K2	3, 8
TW Hya	11 01 51.91	–34 42 17.0	Prz	9–10	194	K7	1, 3, 9, 10
Glass I ^d	11 08 15.41	–77 33 53.5	Prz	2.5	22/1.4	K4	11–14
WW Cha	11 10 00.7	–76 34 59	Prz	0.3–0.8	66–67	K5	3, 4, 8, 11
Hen 3–600 A	11 10 28.86	–37 32 04.8	K-S	10	12.5	M4	13, 14
IRAS 14050–4109	14 08 10.3	–41 23 53	K-S	...	2.0	K5	13, 15
RU Lup	15 56 42.31	–37 49 15.5	Prz, here	0.1–0.5	136–216	K7–M0	3, 8, 16
AS 205 NE	16 11 31.40	–18 38 24.5	Prz, here	0.1	154.6	K5	2, 17
AS 205 SW	16 11 31.40	–18 38 24.5	Prz, here	<0.1	54.9	K5	2, 17
Do Ar 24E ^d	16 26 17.06	–24 20 21.6	Prz, here	1.5	5	K0	17, 18
Haro 1-16	16 31 33.53	–24 27 33.4	Prz	...	59–76	K2–K3	2, 8, 18
AK Sco	16 54 44.85	–36 53 18.6	Prz	1.0	3–9	F5	3, 13, 19
S CrA NW	19 01 08.60	–36 57 20.0	Prz	3.0	73.0	K3	13, 17
S CrA SE	19 01 08.60	–36 57 20.0	Prz	1.0	61	MO	13, 17
MWC 480	04 58 46.27	+29 50 37.0	K-S	5–6	18.3	A2–A3	1, 20–23
UX Ori A	05 04 29.99	–03 47 14.3	vB	3–5	20.0	A2–A3	1, 19, 20–23
HD 37357	05 37 47.08	–06 42 30.2	vB	A0	22
HD 37806	05 41 02.29	–02 43 00.7	vB	6.3	...	B9–A2	22–24
HD 95881	11 01 57.62	–71 30 48.4	vB	...	21.1	A1–A2	21, 22
HD 98922	11 22 31.67	–53 22 11.5	vB, here	...	27.9	B9	21, 22
HD 101412	11 39 44.46	–60 10 27.7	vB	...	14–20	B9.5	13, 21, 22
HD 104237	12 00 05.08	–78 11 34.6	vB	2	24.3	A4	13, 20–23, 25
HD 142666	15 56 40.02	–22 01 40.0	vB	10	0.8–3	A7–A8	13, 20–22
HD 144432	16 06 57.96	–27 43 09.8	vB	...	5–9	A7–F0	13, 21–24
HD 150193	16 40 17.92	–23 53 45.2	vB	3–5	5	A0–A4	20–22, 25
HD 163296	17 56 21.29	–21 57 21.9	vB, K-S, here	5	14.5	A0–A2	1, 21–23, 26
HD 179218	19 11 11.25	+15 47 15.6	K-S	0.1	18.2	B9–A0	21–23
WW Vul	19 25 58.75	+21 12 31.3	K-S	>10	18–24	B9–A3	3, 4, 20–22
HD 184761	19 34 58.97	+27 13 31.2	K-S	A8	27

NOTE.—Sources up to and including S CrA SE are TTs; sources after S CrA SE are HAEBEs.

^a Units of right ascension are hours, minutes, and seconds, and units of declination are degrees, arcminutes, and arcseconds; the R.A. and Decl. quoted here were obtained from SIMBAD and do not necessarily represent the position of the referenced MIR spectroscopic observations.

^b References for silicate spectroscopy: vB = van Boekel et al. 2003; Prz = Przygodda et al. 2003; K-S = Kessler-Silacci et al. 2005; here = this paper.

^c All H α lines are in emission.

^d This source is a binary that is unresolved in the referenced MIR spectroscopic observations. Stellar/disk parameters quoted from the literature include both sources.

REFERENCES.—(1) Thi et al. 2001; (2) Cohen & Kuhl 1979; (3) Reipurth et al. 1996; (4) Hartmann et al. 1998; (5) Strom et al. 1989; (6) Poncet et al. 1998; (7) Levrault 1988; (8) Appenzeller et al. 1983; (9) Webb et al. 1999; (10) Torres et al. 2003; (11) Lawson et al. 1996; (12) Gauvin & Strom 1992; (13) Gregorio-Hetem et al. 1992; (14) Chen et al. 1997; (15) Gregorio-Hetem & Hetem 2002; (16) Hughes et al. 1994; (17) Prato et al. 2003; (18) Bouvier & Appenzeller 1992; (19) Herbig & Bell 1988; (20) Natta et al. 1997; (21) Acke et al. 2005; (22) The et al. 1994; (23) van den Ancker et al. 1998; (24) Meeus et al. 2001; (25) van den Ancker et al. 1997; (26) Finkenzeller & Mundt 1984; (27) Miroshnichenko et al. 1999.

models indicate grain sizes of up to 1.3 times those of homogeneous spheres for features of the same strength. Both mixture models indicate that the largest changes in the shape of the feature occur over a small range of grain sizes, from approximately 1 to 3 μm , with exact values depending on the model used. For the weakest silicate features ($S_{\text{peak}}^{10\mu\text{m}} \leq 1.7$), large changes in grain size result in only small variations in the strength/shape of the silicate feature. Therefore, it becomes increasingly difficult to determine exact grain sizes for the weakest silicate features.

The data discussed above cannot be explained purely by size variations, and in some cases can indeed be attributed to crystalline silicates and/or PAH emission. For the largest grain sizes, Figure 9a shows several spectra with 11.3-to-9.8 μm ratios that consistently lie above the modeled ratios. These data may indicate the presence of crystalline forsterite or PAH emission in the

11.2–11.3 μm region. For a cutoff at $S_{11.3}/S_{9.8} = 1.0$, we find that 13 sources in our sample satisfy this criterion and thus require emission near 11.3 μm that is in excess above models of amorphous olivines/pyroxenes, indicating that the features arise from crystalline silicates or PAHs. These sources are marked with a Y in column (3) of Table 2. Of these 13 sources, 4 show clear evidence of crystalline silicate emission at $\lambda > 25 \mu\text{m}$ (Do Ar 24E, [GY92] 23, hereafter GY 23, HD 98922, and DL Cha). Clear evidence for PAH emission features in the SL spectra can be seen in three additional sources (Lk H α 330, IRAS 03446+3254, Haro 1-17, and HD 135344). The spectra of three more sources (VSSG1, Lk H α 327, and RR Tau) show evidence of both PAH and crystalline silicate features. The remaining three sources with $S_{11.3}/S_{9.8} > 1.0$ (T Cha, EM* SR21, hereafter SR 21, and HD 135344) display narrow isolated 11.3 μm emission and

have very simple spectra that show only shallow $\sim 20 \mu\text{m}$ silicate emission. This likely indicates that the $11.3 \mu\text{m}$ features in these three spectra arise from PAH, and not crystalline silicate, emission. Therefore, for all of the spectra with $S_{11.3}/S_{9.8} > 1.0$, the additional flux at $11.3 \mu\text{m}$ can indeed be explained by crystalline silicate and/or PAH emission. The nature of the $11.3 \mu\text{m}$ features and relationship to PAH emission will be discussed more thoroughly in V. Geers et al. (2006, in preparation). Aside from the spectra with $S_{11.3}/S_{9.8} > 1.0$, the data presented in Figure 9a are consistent with grain size variations.

The $20 \mu\text{m}$ features show a shape-strength trend that is very similar to that seen for the $10 \mu\text{m}$ features (Fig. 9b). Here we use the ratio of the flux at 23.8 to $19 \mu\text{m}$ —again, the peaks of the most prominent amorphous and crystalline silicate features—as a proxy for the feature shape. This plot includes only c2d data, as continuum-normalized *ISO* data were not available. The paucity of spectra with strong $20 \mu\text{m}$ features may be related to the prominence of weak, flat $10 \mu\text{m}$ features in the c2d sample, indicating large grain sizes. Although the sample size (and range in peak strength) is smaller for the $20 \mu\text{m}$ features, the shape-strength trend is still prominent. This trend possesses a similar slope and y -intercept to that seen for the $10 \mu\text{m}$ features and is again most closely matched with the Mie model of an olivine-pyroxene mixture, which agrees to within $S_{23.8}/S_{19} = 0.01$, or $\sim 1\%$. There appears to be little difference in grain composition between grains being probed by the 10 and $20 \mu\text{m}$ features.

All of the $20 \mu\text{m}$ features are consistent with models of amorphous olivine-pyroxene mixtures of sizes between 0.1 and $20 \mu\text{m}$, with no deviations indicative of strong crystalline features. A similar fit is obtained for the Mie and DHS models of the olivine-pyroxene mixture, but for the DHS models much larger grain sizes ($a > 20 \mu\text{m}$) are needed. The data are also consistent with DHS and Mie models of amorphous olivines (to within $S_{23.8}/S_{19} = 0.08$, or $\sim 8\%$) for much smaller grain sizes ($a \leq 5 \mu\text{m}$). This makes exact grain size determination difficult. Furthermore, a large scatter in the modeled data points can be seen for $S_{20 \mu\text{m}}^{\text{peak}} < 1.1$ due to difficulties in fitting the continuum for such weak features. This prevents identification of small deviations in feature shape between the models and data for large grain sizes (as were seen for the $10 \mu\text{m}$ features). However, larger deviations from the models are not seen. Thus, although there is evidence in some individual spectra for crystalline silicate features, the entire trend is consistent with amorphous olivine-pyroxene mixtures with source-to-source size variations.

For the 48 sources observed in this study, the 10 and $20 \mu\text{m}$ features both exhibit strength-shape trends consistent with source-to-source grain size variations, with most of the observed features similar to models of grains with sizes much larger than that of the ISM ($a \gg 0.1 \mu\text{m}$). This indicates that grain growth must occur quickly in these disks. Furthermore, as the observed features arise from silicate emission in the disk surface layers, and the largest grains will gravitationally settle to the disk midplane, the emitting grains likely represent the low-size tail of the silicate grain size distribution within the disk. This effect is enhanced by the fact that larger grains have weaker silicate emission features.

5.2. 10 Versus 20 μm Feature Strengths

One of the most interesting aspects of this sample is a set of sources with very strong $S_{10 \mu\text{m}}^{\text{peak}}$ but weak $S_{20 \mu\text{m}}^{\text{peak}}$. These “outliers” can be clearly seen in a plot of the strengths of the 10 and $20 \mu\text{m}$ features in the observed spectra (Fig. 10). The feature strengths appear to be correlated over the entire sample ($r = 0.36$, 96% probability of correlation). However, examination of Figure 10a

reveals that the bulk of the data are clustered around $S_{20 \mu\text{m}}^{\text{peak}} \approx 1.3$ and $S_{10 \mu\text{m}}^{\text{peak}} \approx 1.5$, and ~ 11 outliers have 10 and $20 \mu\text{m}$ features with very different strengths. Furthermore, most of these outliers have strong $10 \mu\text{m}$ features ($S_{10 \mu\text{m}}^{\text{peak}} > 2$) and weak $20 \mu\text{m}$ features ($S_{20 \mu\text{m}}^{\text{peak}} < 1.6$). No sources in our sample have strong $10 \mu\text{m}$ features and equally strong $20 \mu\text{m}$ features. One may expect weak $20 \mu\text{m}$ features to be more abundant, as most sources show weak $10 \mu\text{m}$ features (see Fig. 9a), and grain growth is occurring quickly in these disks. However, the fact that there are *no* sources with strong $20 \mu\text{m}$ features and weak $10 \mu\text{m}$ features is significant.

In order to interpret the distribution of peak strengths in the observed spectra, we examine the effect of a variety of grain parameters on the strengths of the 10 and $20 \mu\text{m}$ features. Factors affecting silicate feature strengths include, but are not limited to, the grain size distribution, relative sizes of grains emitting at 10 and $20 \mu\text{m}$, grain composition, crystallinity, and porosity. We attempt to assess the influence of each of these parameters in Figures 10b–10f, Table 5, and §§ 5.2.1–5.2.3 for models of normalized Q_{abs} calculated as described in § 4.2.

5.2.1. Grain Size Distributions

The effects of grain size are explored by modeling opacities for a set of grains with a differential grain size distribution $dn(a) \propto a^{-p} da$ and varying the minimum grain size a_{min} , maximum grain size a_{max} , and power-law index p , as shown in Figure 10b. All three parameters have very similar effects; increasing a_{min} or a_{max} or decreasing p results in more large grains and reduces both the 10 and $20 \mu\text{m}$ feature strengths, but does not affect the ratio of the two. Thus, variation of the grain size distribution cannot account for the extreme 10 -to- $20 \mu\text{m}$ ratios of the outliers in Figure 10a. The bulk of the observed data set is centered around 10 and $20 \mu\text{m}$ feature strengths, similar to that of a grain size distribution with $a_{\text{min}} = 1.0 \mu\text{m}$, $a_{\text{max}} = 100 \mu\text{m}$, and power-law index $p = 3.5$.

The emission at 10 and $20 \mu\text{m}$ likely comes from different populations of grains. This is a simple consequence of the temperature dependence of the emission as a function of wavelength (e.g., emission at $20 \mu\text{m}$ can arise from colder grains than emission at $10 \mu\text{m}$). We therefore expect the contribution of a particular grain to the 10 and $20 \mu\text{m}$ features to depend on the location of the grain. In order to determine the relative contribution of grains from different radii to the 10 and $20 \mu\text{m}$ features, we perform an exercise using a simple two-layer model (CGPLUS; Dullemond et al. 2001; Chiang & Goldreich 1997) to calculate the cumulative disk flux as a function of radius at 10 and $20 \mu\text{m}$ for a typical TT. Figure 11 shows that the radii probed by the 10 and $20 \mu\text{m}$ silicate features can indeed be quite different, with the $20 \mu\text{m}$ feature probing radii up to 10 times those probed by the $10 \mu\text{m}$ feature.

In Figure 10c, the relationship between the sizes of the grains emitting at 10 and $20 \mu\text{m}$ is explored. We vary a_{min} for the models of the $20 \mu\text{m}$ feature while keeping a_{max} , p , and a_{min} for the models of the $10 \mu\text{m}$ feature constant. The entire distribution of the data can be reproduced by these models. Most data correspond to $a_{\text{min}}^{10 \mu\text{m}} = 1 \mu\text{m}$ and $a_{\text{min}}^{20 \mu\text{m}} = 0.1\text{--}3 \mu\text{m}$, but the data on the right side of Figure 10c require large differences between the sizes of grains emitting at 10 and $20 \mu\text{m}$ ($a_{\text{min}}^{10 \mu\text{m}} = 0.1 \mu\text{m}$ and $a_{\text{min}}^{20 \mu\text{m}} = 2\text{--}3 \mu\text{m}$).

The 10 and $20 \mu\text{m}$ features are clearly probing different dust populations. The bulk of the data can be reproduced by models of $1.0 \mu\text{m}$ grains, indicating significant growth in these disks compared to the ISM. Although the data are clustered and centered around the dashed lines that denote equal grain sizes for 10 and $20 \mu\text{m}$ emission, many spectra can be better represented by much larger grains emitting at $20 \mu\text{m}$ than at $10 \mu\text{m}$. This may be

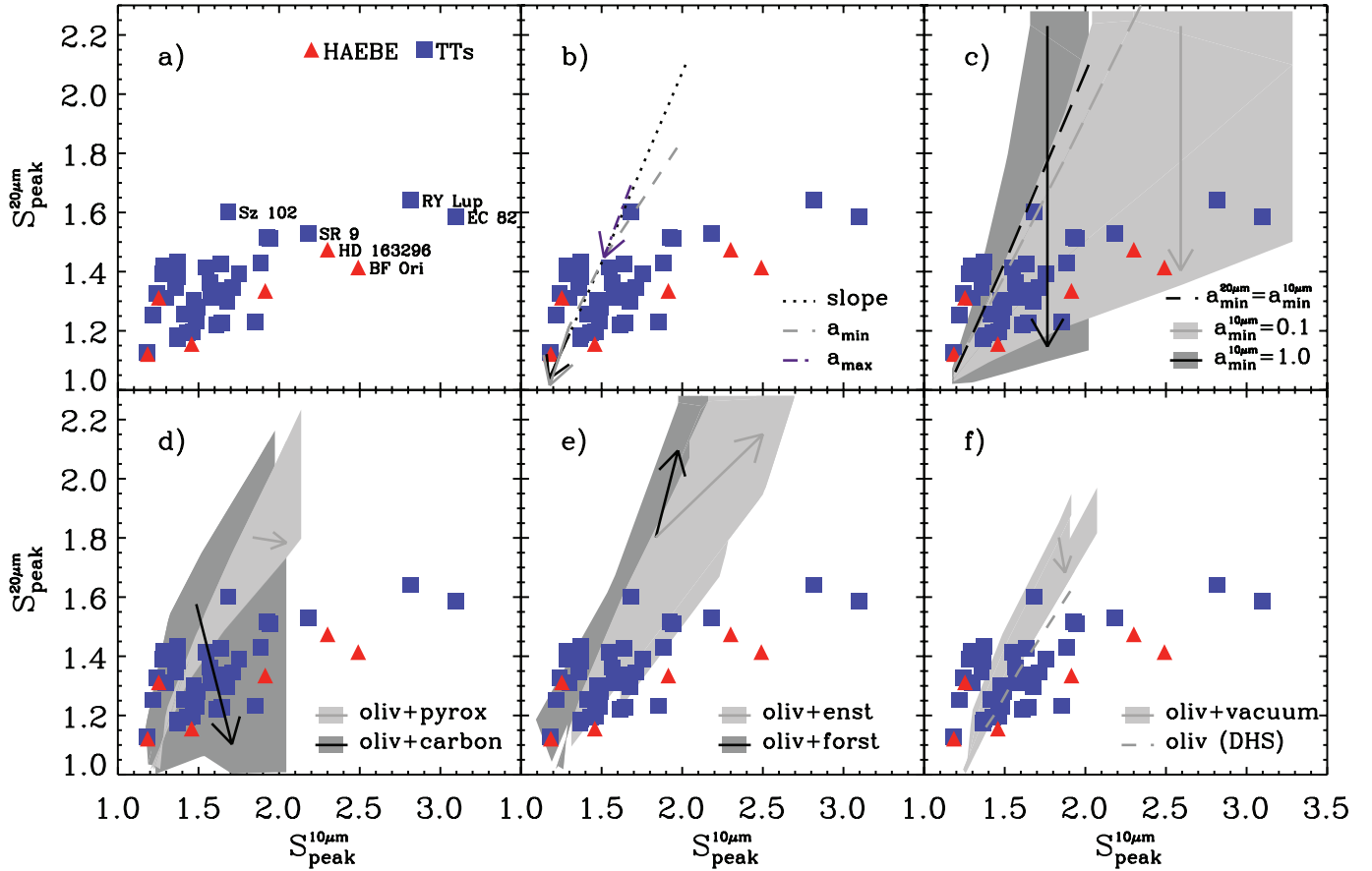


FIG. 10.—(a) Relative strengths of the 20 vs. 10 μm features. Models are overplotted showing variations in (b) grain size distribution, (c) ratios of grain sizes emitting at 10 and 20 μm , (d) grain composition, (e) crystallinity, and (f) porosity. The reference opacities are calculated via Mie theory for pure olivine grains with differential grain size distributions with $a_{\text{min}} = 1.0 \mu\text{m}$, $a_{\text{max}} = 100 \mu\text{m}$, and power-law index $p = -3.5$ for both the 10 and 20 μm features. Arrows in (b) indicate the direction of increasing slope p , a_{min} , and a_{max} . Gray shaded regions in (c) indicate the range in 10 and 20 μm feature strengths covered by variations in $a_{\text{min}}^{20\mu\text{m}}$ with $a_{\text{min}}^{10\mu\text{m}} = 0.1 \mu\text{m}$ and $a_{\text{min}}^{10\mu\text{m}} = 1.0 \mu\text{m}$. Arrows in (c) indicate the direction of increasing 10-to-20 μm grain size ratios over the gray shaded regions. Gray shaded regions in (d)–(f) indicate the range in 10 and 20 μm feature strengths covered by variations in $x/\text{olivine}$ ratios, where x is (d) pyroxene or amorphous carbon, (e) forsterite or enstatite, and (f) vacuum for grains of constant size. Arrows in (d)–(f) indicate the direction of increasing $x/\text{olivine}$ ratios. Symbols are defined as in Fig. 9.

TABLE 5
MODEL PARAMETERS FOR FIGURE 10

Panel	Parameter	Variables	Range
b.....	Size distribution ^a	a_{min}	0.01–3.0 μm
		a_{max}	10–100 μm
		p	4.5–2.5
c.....	Sizes for 10 vs. 20 μm	p	4.5–2.5
		a_{min}^{10}	0.1, 1.0 μm
		a_{min}^{20}	(0.1–20) \times 0.1 μm
		a_{min}^{20}	(0.5–3) \times 1.0 μm
d.....	Composition	$a_{\text{min}}^{10} = a_{\text{min}}^{20}$	0.01–3.0 μm
		Olivine : carbon	100 : 0–50 : 50
e.....	Crystallinity	Olivine : pyroxene	100 : 0–0 : 100
		$a_{\text{min}}^{10} = a_{\text{min}}^{20}$	0.01–3.0 μm
		Olivine : forsterite	100 : 0–0 : 100
f.....	Porosity	Olivine : enstatite	100 : 0–0 : 100
		$a_{\text{min}}^{10} = a_{\text{min}}^{20}$	0.01–3.0 μm
		Olivine : vacuum	100 : 0–20 : 80

^a Using a differential grain size distribution of $dn(a) \propto a^{-p} da$, where the absorption efficiency is defined as $\langle Q_{\text{abs}} \rangle = \int_{a_{\text{min}}}^{a_{\text{max}}} Q_{\text{abs}} dn(a) / \int_{a_{\text{min}}}^{a_{\text{max}}} dn(a)$.

explained, if the emission is optically thin, by a difference in the $\tau = 1$ surface depth as a function of wavelength of the emission; 20 μm features probe a deeper layer of the disk, where grain sizes are likely larger due to larger density and dust settling. One would also expect, however, that dust at larger radii (and lower temperature), which is likely smaller due to decreased densities, contributes more to the 20 μm feature than to the 10 μm feature. There is thus a competing effect between the disk height and radius being probed. This may explain why most of the data points are centered around the dashed lines that denote equal grain sizes for 10 and 20 μm emission. In the case of the outliers, enhanced dust settling may make the disk-height differential between dust probed by the two features more important than the difference in radius.

5.2.2. Grain Composition and Crystallinity

Grain composition and crystallinity also affect the strengths of the silicate emission features, resulting in ranges of peak strengths that are very similar to those produced by varying the grain sizes (with $a_{\text{min}}^{10\mu\text{m}} = a_{\text{min}}^{20\mu\text{m}}$). Thus, effects of grain size variation, composition, and crystallinity are difficult to disentangle using 10-to-20 μm flux ratios.

In Figure 10d, we vary the percentage of amorphous pyroxene and amorphous carbon relative to amorphous olivine. To simplify matters, we use the same composition and grain sizes for

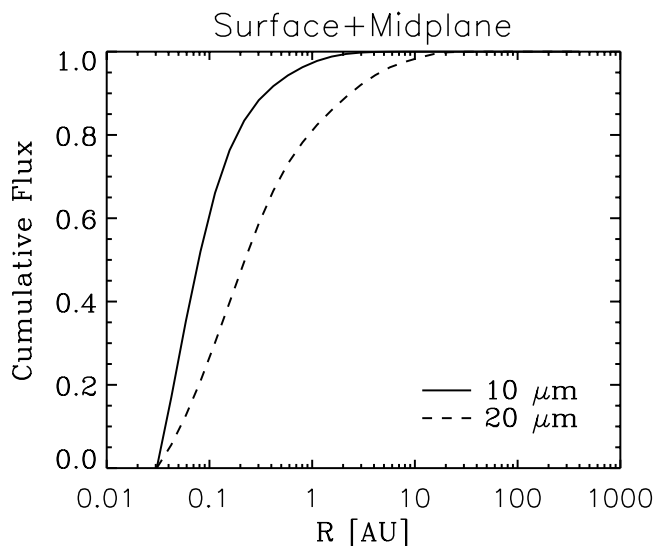


Fig. 11.—Cumulative flux at 10 μm (solid line) and at 20 μm (dashed line) as a function of radius. Fluxes are calculated using the CGPLUS model (Dullemond et al. 2001) for a disk around a TT with $T_* = 4000\text{ K}$, $L_* = 0.58 L_\odot$, containing olivine grains of a differential grain size distribution with $a_{\min} = 1\ \mu\text{m}$, $a_{\max} = 100\ \mu\text{m}$, and $p = -3.5$. Of the 10 μm flux, 95% comes from within $\sim 1\text{ AU}$, while 95% of the 20 μm flux comes from within $\sim 10\text{ AU}$.

the grains emitting at 10 and 20 μm . Increasing the pyroxene-to-olivine fraction has the largest effects for small grains ($< 1.0\ \mu\text{m}$), resulting in an increased 10 μm feature strength and roughly constant 20 μm feature strength (as seen previously in Fig. 9). Increasing the carbon-to-olivine fraction has an even larger effect on grains of small sizes, with a larger effect on the 20 μm feature than the 10 μm feature, as the peak-to-continuum ratio is decreased due to an increase in the effective continuum.

Variations in crystallinity (using DHS models) also result in the same range of peak strengths, but highly crystalline grains can produce features with the same peak strengths at smaller grain sizes (Fig. 10e). When the fraction of forsterite or enstatite is less than $\sim 50\%$, the feature strengths remain very similar to amorphous olivine. Beyond a crystalline fraction of $\sim 50\%$, the strong and narrow crystalline emission features begin to dominate, and the strengths of the peak emission in the 10 and 20 μm regions appear to increase dramatically for the same grain size distribution. For models of $> 50\%$ crystalline forsterite and enstatite, the gray shading in Figure 10e extends far beyond the plotted range of the y-axis ($S_{\text{peak}}^{20\ \mu\text{m}} \gg 2.28$). Thus, for primarily crystalline grains, grain size distributions with $a_{\min} \leq 2.0\ \mu\text{m}$ can account for the entire gray area shown.

Differing composition and crystallinity can account for the 10 and 20 μm ratios of the bulk of the observed spectra, but not the outliers. In addition, the 10 and 20 μm ratios of models of varying grain composition and crystallinity encompass ranges in which no observational data lie. In particular, spectra showing weak 10 μm features ($S_{\text{peak}}^{10\ \mu\text{m}} > 1.7$) and strong 20 μm features can be easily produced with models of small-sized ($a_{\min} < 1.0\ \mu\text{m}$) amorphous silicate/carbonaceous grains or moderately sized ($a_{\min} < 3.0\ \mu\text{m}$) crystalline silicate grains, but they are not seen in the c2d sample. These absences confirm the idea that the 20 μm feature probes regions of larger grain size than does the 10 μm feature, irrespective of grain composition and crystallinity.

5.2.3. Dust Porosity

Finally, in Figure 10f we explore the effects of grain opacity by increasing the vacuum fraction of a set of olivine grains and

by using the DHS method. In both cases, we integrate over a grain size distribution, as in Figures 10d–10e. The primary difference between the two methods is that the opacities calculated with DHS are the average of a set of hollow spheres of varying vacuum fractions for a given mass, which is translated to grain size. The Q_{abs} are then integrated over a grain size distribution. For the olivine+vacuum grains, the opacities and Q_{abs} are calculated and integrated over grain size for each volume fraction individually. The variation over vacuum fraction (Fig. 10f, light gray) does not have a large effect on the 10-to-20 μm ratio and is consistent with the DHS 10 and 20 μm strengths and variation with a_{\min} . Variations in dust porosity can only explain a fraction of the bulk of the sample, which overlaps with the regions covered by models of varying grain composition, and cannot explain the outliers. Thus, it is not necessary to consider porosity to explain the observed 10 and 20 μm feature strengths.

6. GRAIN GROWTH AND STELLAR/DISK PROPERTIES

In order to evaluate the dependence of the strength-shape trend noted in § 5 on stellar and disk parameters, we plot the 10 μm shape versus strength again in Figures 12a–12c, color-coded by spectral type, stellar age, and H α equivalent width (for TTs only). Stellar/disk parameters for each source observed in this study (c2d) were collected from the literature and are shown in Table 1. Stellar/disk parameters for 10 μm data obtained from van Boekel et al. (2003), Przygodda et al. (2003), and Kessler-Silacci et al. (2005; lit) are shown in Table 4. We evaluate the probability that the sets of spectral type, stellar age, or H α equivalent width bins are drawn from the same distribution on the 10 μm feature shape-strength relation shown in Figure 9a by evaluating the two-sided Kolmogorov-Smirnov (K-S) statistic (D) for each stellar/disk parameter.¹⁴ As we are evaluating the dependence of the strength-shape trend on stellar/disk parameters, we use only the sources with $S_{11.3}/S_{9.8} < 1.0$, thus removing sources with substantial emission from crystalline silicates and/or PAHs. Some stellar/disk parameters are not available in the literature, and therefore not all sources are included in Figures 12a–12c.

6.1. Spectral Type

As the data in our sample (Fig. 12, filled symbols) appear to be consistent with the largest silicate grain sizes, and probe disks around primarily K and M stars, we first looked for connections between grain size and spectral type. We divide the sample by spectral type into four groups: (1) A/B, (2) F/G, (3) K, and (4) M. The A and B stars and F and G stars were combined into single groups, as few stars of each type were observed. The K-S test is used to compare two arrays of data values, and the process is repeated for each combination of groups 1–4. In general, there appears to be a dependence on spectral type, with A/B stars being clustered toward the middle and lower right of the 10 μm feature strength-shape trend and M stars being more clustered toward the upper left region of Figure 12. This can be more easily seen in Figure 13, where histograms of the 10 μm shape-to-strength ratio for A/B stars and M stars are compared. The population of A/B stars peaks at ratios near 0.1 and decreases for larger ratios, while only a few M stars have shape-to-strength ratios near 0.1 and the population increases for larger ratios to peak near 0.5–0.6.

Although it appears that 10 μm silicate emission may be different in A/B stars versus M stars, a larger data set is needed

¹⁴ The two-sided K-S statistic is the difference between the cumulative distribution function (CDF) of two sets of data and is calculated using KSTWO (Press et al. 1992).

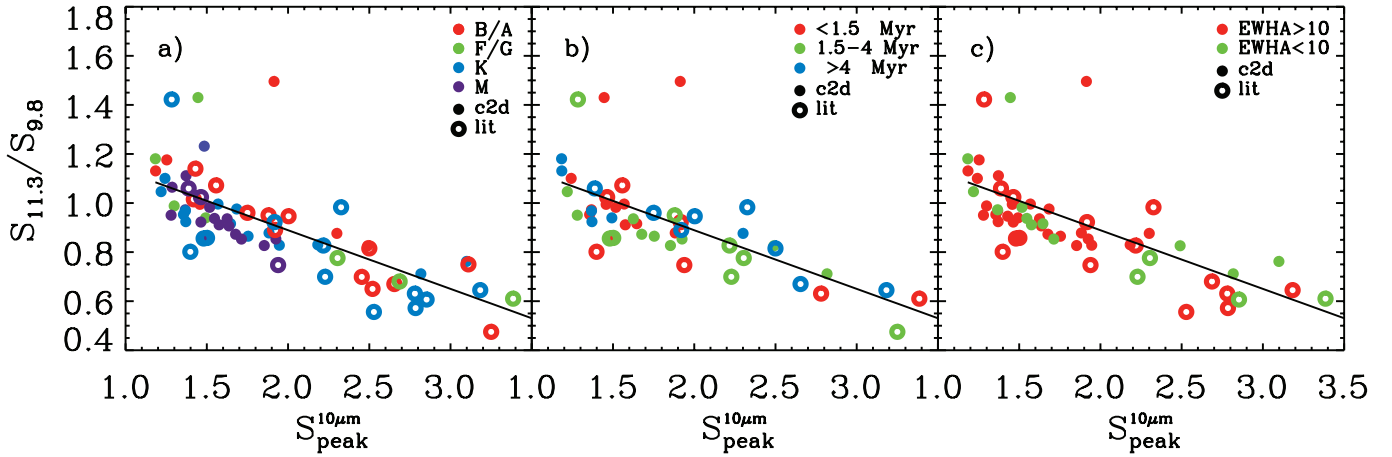


FIG. 12.—Shape and strength of the $10\ \mu\text{m}$ silicate features. The shape of the feature ($S_{11.3}/S_{9.8}$) is plotted vs. the feature strength ($S_{10\ \mu\text{m}}^{\text{peak}}$) in all panels. The points are color-coded by (a) spectral type, (b) age, and (c) H α EW. Silicate features from the literature (van Boekel et al. 2003; Przygodda et al. 2003; Kessler-Silacci et al. 2005) are represented by open symbols. The black line in all panels indicates the correlation found for the $10\ \mu\text{m}$ features shown in Fig. 9a, including all observations. This trend is not strongly dependent on H α EW or age, but may be related to spectral type.

to confirm this result. The calculated probabilities that these groups are drawn from the same distribution range from 15% ($D = 0.29$) for spectral types A/B and M, to 98% ($D = 0.17$) for spectral types A/B and F/G. Objects that are close in spectral type, in subsequent groups (e.g., 1 vs. 2, 2 vs. 3), have large probabilities (69%–98%) of being drawn from the same distribution. Groups with larger differences in spectral type (e.g., 1 vs. 3, 2 vs. 4) have smaller probabilities (15%–50%). Of all these comparisons, however, only the K-S test for group 1 versus 4 (A/B vs. M) indicates a low-enough probability ($\leq 20\%$; Press et al. 1992) to suggest that the differences in the populations are statistically significant. Furthermore, the number of objects in each group is still quite low (13 A/B stars, 4 F/G stars, 24 K stars, and 15 M stars), and the spectral types typically have errors on the order of 3 subclasses.

The dependence of the strength-shape trend on spectral type may be explained in terms of the disk temperature and density structure. If we assume that the $10\ \mu\text{m}$ feature always probes

grains of roughly the same temperature, then the radius being probed by the $10\ \mu\text{m}$ emission will change as a function of the temperature structure of the disk. The disk temperature $T(R)$ varies as a function of radius as (from Dullemond & Dominik 2005)

$$T(R) = \alpha^{1/4} \sqrt{\frac{R_*}{R}} T_*,$$

where α is the disk flaring angle and R_* and T_* are the stellar radius and temperature. R is the radius corresponding to temperature $T(R)$, in this case the dominant radius being probed by the silicate emission feature, which we call R_{sil} . Assuming that $T(R_{\text{sil}})$ and α are constant over the entire disk sample, and using typical values of R_* and T_* for A/B and M stars, $R_{\text{sil,A/B}}/R_{\text{sil,M}} \approx 10$ –25. So the radius probed by the $10\ \mu\text{m}$ emission feature is quite different for stars of spectral types A/B and M. Furthermore, the density generally increases with decreasing radius, and grain growth increases at higher density, while dust settling decreases at higher density. Thus, the combination of faster grain growth and slower dust settling at smaller radii could lead to the larger grains that we see in M stars versus A/B stars. Although this simple theory is consistent with the observed correlation of grain size with spectral type, several other spectral-type-dependent factors (e.g., X-rays, UV radiation, and stellar/disk winds) likely influence grain size in these disks.

6.2. Age

Although one might expect grain growth and crystallization to occur over time, as the disk matures, we see no clear relationship between the strength-shape trend and stellar age (Fig. 12b). The ages for our sample are culled from the literature and range from 0.5 to 6 Myr, with errors of up to a few Myr (i.e., Hillenbrand & White 2004). We therefore divide up the sample into three approximately equally sized groups—stars with ages of (1) <1.5 Myr, (2) 1.5–4 Myr, and (3) >4 Myr—and follow a similar method as described above for the analysis of spectral type. The strength-shape trend does not appear to be strongly related to the age of the star (Fig. 12b), with probabilities of $>47\%$ that all three groups are drawn from the same distribution. However, this analysis would be more conclusive for stars within one cluster with a well-defined age, for which relative ages could be more accurately determined. With the available ages, these results indicate that the

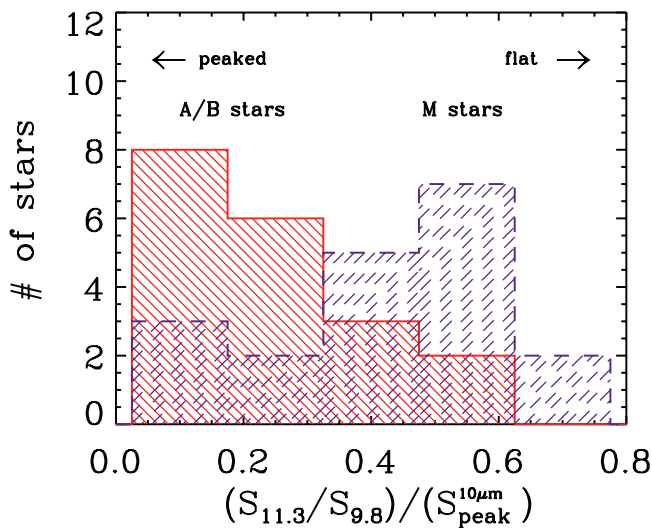


FIG. 13.—Histogram of the $10\ \mu\text{m}$ feature shape-to-strength ratios for the A/B and M stars shown in Fig. 12a. Spectra of A and B stars show more centrally peaked $10\ \mu\text{m}$ features, lying in the middle and left regions of Fig. 12a, while spectra of M stars show primarily flattened features, lying in the upper left region of Fig. 12a. The bin widths are 0.1 in units of $(S_{11.3}/S_{9.8})/(S_{10\ \mu\text{m}}^{\text{peak}})$.

stellar age of pre-main-sequence (PMS) stars is not directly related to the state of the small, micron-sized grains in these disks.

In addition to the difficulties in determining the disk age, the lack of an age dependence of the shape-strength trend can be understood when grain fragmentation and disk turbulence are considered. Dullemond & Dominik (2005) found that in models including only basic coagulation mechanisms, grain growth occurs very quickly, such that the SEDs show much weaker IR excess (even at young ages of 1 Myr) than do disks around most classical TTs. The settling of small grains, removing them from the disk surface, occurs over even faster timescales. The lack of sources with strongly peaked 10 μm features (and therefore small grains) in the substantial sample observed here is consistent with this fast timescale for grain growth (to 1 μm sizes). The presence of strongly peaked 10 μm features in some sources (particularly in the lit sample) may be indicative of the replenishment of small grains in disk surface layers through mechanisms such as fragmentation and/or turbulent mixing. (Some amount of large grains will also be mixed into disk surface layers.) The models presented in Dullemond & Dominik (2005) suggest that such mechanisms may allow disk systems to maintain quasi-stationary grain size distributions, with grain growth and small-grain replenishment rates in equilibrium for long periods of time (≥ 1 Myr). Thus, the typical grain sizes found in disks around PMS stars are likely not to be directly related to disk age, but indicative of a number of other factors, such as the strength of the turbulence and the gas mass in the disk.

6.3. Accretion

We also do not see a correlation of the strength-shape trend with the equivalent width of the H α emission lines (H α EW) probing disk evolution (Fig. 12c). The H α EW is a tracer of active stellar accretion from the inner disk. Thus, clearing of the inner disk will result in lower H α EW. In Figure 12c, we separate the TTs in our sample into two groups, using the equivalent width of H α : 35 classical TTs (cTTs; H α EW > 10 Å) and 14 weak-lined TTs (wTTs; H α EW < 10 Å). Although there is no clear observational evidence that cTTs are progenitors of wTTs, wTTs are often described as cTTs in which the inner disk has dissipated. Therefore, we might expect that the clearing of the inner disk, and thus the transition between the classical and weak-line TT phases, would be related to grain growth and the 10 μm feature strength-shape trend. We find that there is a high probability ($\sim 70\%$) that the two groups are drawn from the same distribution, however, indicating that there is no clear relationship between H α EW and grain growth in these disks. This indicates either that H α EW is not a good probe of the disk evolutionary state or stellar accretion rate, or that grain growth is not related to these quantities. We also note that H α emission can be quite variable, and the values used here are time averages, using the full range of observed H α EW as error bars. The relation between H α EW and silicate feature shape-strength would be more precisely tested with simultaneous MIR and optical spectroscopy.

7. CONCLUSIONS

Spectra in the ~ 5 – 35 μm region have been obtained for disks around 40 TTs and 7 HAEBEs using the *Spitzer Space Telescope*, as a subset of the c2d IRS survey. This is the first significant sample of T Tauri stars for which both 10 and 20 μm features are available. Broad silicate features at 10 and 20 μm , similar to emission from amorphous silicates, are prominent toward the observed sample of TTs and HAEBEs. Emission

features from crystalline silicates are also evident in the observed spectra, with the most prominent features visible in the 33–36 μm region.

We performed a statistical analysis of the shapes and strengths of the 10 and 20 μm features and find the following.

1. If the full IRS spectra are considered, the data are most consistent with source-to-source variations in grain size, with the bulk of the sources in our sample indicating sizes of 1 μm or greater. This and the lack of strongly peaked 10 μm sources in our sample of 40 sources is consistent with fast grain growth (from 0.1 to 1.0 μm sizes) in the surfaces of these disks.

2. Long-wavelength (33–36 μm) crystalline silicate features are seen toward approximately half of the TT disks in our sample. This indicates that significant dust processing is also occurring in these disks. Only 13 of these spectra also exhibit 11.3-to-9.8 μm ratios that cannot be reproduced by models of amorphous silicates, suggesting that the degree of crystallinity deduced from the 10 μm region alone is underestimated.

3. A subset of the observed spectra has particularly large 10-to-20 μm ratios, which can only be reproduced with much smaller grains emitting at 10 μm ($a_{\text{min}} = 0.1$ μm) than at 20 μm ($a_{\text{min}} = 2$ – 3 μm). This can be explained if the 20 μm emission arises from deeper in the disk than the 10 μm emission in disks where dust settling has occurred.

4. The 10 μm feature strength versus shape trend is *not* correlated with age or disk evolutionary state (H α EW). This suggests the importance of turbulence and the regeneration of small (micron-sized) grains on the disk surface.

5. The 10 μm feature strength versus shape trend is related to spectral type, with M stars showing significantly flatter silicate features (larger grain sizes) than those of A/B stars. This may be related to a difference in the radius probed by the emission, which should increase as a function of the disk temperature and thus stellar luminosity. However, the observed correlation could also be indicative of other spectral-type-dependent factors (e.g., X-rays, UV radiation, and stellar/disk winds).

As the observed features arise from silicate emission in the disk surface layers, and the largest grains will gravitationally settle to the disk midplane, the emitting grains likely represent the small-size tail of the silicate grain size distribution within the disk. This simple picture of grain growth and settling is complicated by vertical mixing, which can bring both large and small grains back to the disk surface, and fragmentation, which results in the replenishment of small grains throughout the disk. Comparisons with probes of grain size in the disk midplane and inner disk clearing, as well as probes of disk turbulence and gas-dust interactions, are vital to understanding the results presented here in the context of planet formation.

Support for this work, part of the *Spitzer Space Telescope* Legacy Science Program, was provided by NASA through contracts 1256316, 1224608, and 1230780, issued by the Jet Propulsion Laboratory, California Institute of Technology, under NASA contract 1407. Astrochemistry in Leiden is supported by a NWO Spinoza and NOVA grant, and by the European Research Training Network The Origin of Planetary Systems (PLANETS, contract HPRN-CT-2002-00308). The authors would like to thank Michiel Min for communicating his results on DHS, and Jeroen Bouwman, Thomas Henning, Roy van Boekel, Rens Waters, Antonella Natta, David Koerner, and the ApJ referee for helpful comments and suggestions.

REFERENCES

- Acke, B., & van den Ancker, M. E. 2004, *A&A*, 426, 151
- Acke, B., van den Ancker, M. E., & Dullemond, C. P. 2005, *A&A*, 436, 209
- Alcala, J. M., Krautter, J., Schmitt, J. H. M. M., Covino, E., Wichmann, R., & Mundt, R. 1995, *A&AS*, 114, 109
- Appenzeller, I., Krautter, J., & Jankovics, I. 1983, *A&AS*, 53, 291
- Bouvier, J., & Appenzeller, I. 1992, *A&AS*, 92, 481
- Bouwman, J., Meeus, G., de Koter, A., Hony, S., Dominik, C., & Waters, L. B. F. M. 2001, *A&A*, 375, 950
- Bradley, J. 2003, in *Astromineralogy*, ed. T. K. Henning (Berlin: Springer), 217
- Chen, H., Grenfell, T. G., Myers, P. C., & Hughes, J. D. 1997, *ApJ*, 478, 295
- Chiang, E. I., & Goldreich, P. 1997, *ApJ*, 490, 368
- Chiang, E. I., Joungh, M. K., Creech-Eakman, M. J., Qi, C., Kessler, J. E., Blake, G. A., & van Dishoeck, E. F. 2001, *ApJ*, 547, 1077
- Cohen, M., & Kuhl, L. V. 1979, *ApJS*, 41, 743
- D'Alessio, P., Calvet, N., Hartmann, L., Lizano, S., & Cantó, J. 1999, *ApJ*, 527, 893
- D'Alessio, P., et al. 2005, *ApJ*, 621, 461
- Demyk, K., et al. 2001, *A&A*, 368, L38
- Dorschner, J., Begemann, B., Henning, T., Jaeger, C., & Mutschke, H. 1995, *A&A*, 300, 503
- Dullemond, C. P., & Dominik, C. 2004, *A&A*, 417, 159
- . 2005, *A&A*, 434, 971
- Dullemond, C. P., Dominik, C., & Natta, A. 2001, *ApJ*, 560, 957
- Dunkin, S. K., Barlow, M. J., & Ryan, S. G. 1997, *MNRAS*, 286, 604
- Evans, N. J., et al. 2003, *PASP*, 115, 965
- Fernandez, M., Ortiz, E., Eiroa, C., & Miranda, L. F. 1995, *A&AS*, 114, 439
- Finkenzeller, U., & Mundt, R. 1984, *A&AS*, 55, 109
- Gail, H.-P. 1998, *A&A*, 332, 1099
- Gauvin, L. S., & Strom, K. M. 1992, *ApJ*, 385, 217
- Gomez de Castro, A. I. 1997, *A&A*, 323, 541
- Gregorio-Hetem, J., & Hetem, A. 2002, *MNRAS*, 336, 197
- Gregorio-Hetem, J., Lepine, J. R. D., Quast, G. R., Torres, C. A. O., & de La Reza, R. 1992, *AJ*, 103, 549
- Grossman, L. 1972, *Geochim. Cosmochim. Acta*, 36, 597
- Hartigan, P. 1993, *AJ*, 105, 1511
- Hartigan, P., Strom, K. M., & Strom, S. E. 1994, *ApJ*, 427, 961
- Hartmann, L., Calvet, N., Gullbring, E., & D'Alessio, P. 1998, *ApJ*, 495, 385
- Henning, T., Ill'In, V. B., Krivova, N. A., Michel, B., & Voshchinnikov, N. V. 1999, *A&AS*, 136, 405
- Herbig, G. H., & Bell, K. R. 1988, *Catalog of Emission-line Stars of the Orion Population* (Santa Cruz: Lick Obs.)
- Heyer, M. H., & Graham, J. A. 1989, *PASP*, 101, 816
- Higdon, S. J. U., et al. 2004, *PASP*, 116, 975
- Hillenbrand, L. A., & White, R. J. 2004, *ApJ*, 604, 741
- Honda, M., Kataza, H., Okamoto, Y. K., Miyata, T., Yamashita, T., Sako, S., Takubo, S., & Onaka, T. 2003, *ApJ*, 585, L59
- Houk, N. 1982, in *Michigan Spectral Survey* (Ann Arbor: Dept. Astron., Univ. Mich.)
- Hughes, J., & Hartigan, P. 1992, *AJ*, 104, 680
- Hughes, J., Hartigan, P., Krautter, J., & Kelemen, J. 1994, *AJ*, 108, 1071
- Jäger, C., Molster, F. J., Dorschner, J., Henning, T., Mutschke, H., & Waters, L. B. F. M. 1998, *A&A*, 339, 904
- Kemper, F., Vriend, W. J., & Tielens, A. G. G. M. 2004, *ApJ*, 609, 826
- Kenyon, S. J., Brown, D. I., Tout, C. A., & Berlind, P. 1998, *AJ*, 115, 2491
- Kessler-Silacci, J. E., Hillenbrand, L. A., Blake, G. A., & Meyer, M. R. 2005, *ApJ*, 622, 404
- Knacke, R. F., Fajardo-Acosta, S. B., Telesco, C. M., Hackwell, J. A., Lynch, D. K., & Russell, R. W. 1993, *ApJ*, 418, 440
- Lahuis, F., & Boogert, A. 2003, in *SFChem 2002*, ed. C. L. Curry & M. Fich (Ottawa: NRC Press), 335
- Lawson, W. A., Feigelson, E. D., & Huenemoerder, D. P. 1996, *MNRAS*, 280, 1071
- Levrault, R. M. 1988, *ApJ*, 330, 897
- Luhman, K. L., & Rieke, G. H. 1999, *ApJ*, 525, 440
- Martin, E. L., Montmerle, T., Gregorio-Hetem, J., & Casanova, S. 1998, *MNRAS*, 300, 733
- Maxwell Garnett, J. C. 1904, *Royal Soc. London Phil. Trans. A*, 203, 385
- Meeus, G., Waters, L. B. F. M., Bouwman, J., van den Ancker, M. E., Waelkens, C., & Malfait, K. 2001, *A&A*, 365, 476
- Mie, G. 1908, *Ann. Phys.*, 25, 377
- Min, M., Hovenier, J. W., & de Koter, A. 2003, *A&A*, 404, 35
- . 2005, *A&A*, 432, 909
- Miroshnichenko, A. S., Mulliss, C. L., Bjorkman, K. S., Morrison, N. D., Kuratov, K. S., & Wisniewski, J. P. 1999, *MNRAS*, 302, 612
- Molster, F. J., & Waters, L. B. F. M. 2003, in *Astromineralogy*, ed. T. K. Henning (Berlin: Springer), 121
- Natta, A., Grinin, V. P., Mannings, V., & Ungerechts, H. 1997, *ApJ*, 491, 885
- Pollack, J. B. 1984, *ARA&A*, 22, 389
- Pollack, J. B., Hollenbach, D., Beckwith, S., Simonelli, D. P., Roush, T., & Fong, W. 1994, *ApJ*, 421, 615
- Poncet, A., Montes, D., Fernandez-Figueroa, M. J., & Miranda, L. F. 1998, in *ASP Conf. Ser. 154, Cool Stars, Stellar Systems, and the Sun*, ed. R. A. Donahue & J. A. Bookbinder (San Francisco: ASP), 1772
- Prato, L., Greene, T. P., & Simon, M. 2003, *ApJ*, 584, 853
- Press, W. H., Teukolsky, S. A., Vetterling, W. T., & Flannery, B. P. 1992, *Numerical Recipes in FORTRAN* (2nd ed.; Cambridge: Cambridge Univ. Press)
- Przygodda, F., van Boekel, R., Abraham, P., Melnikov, S. Y., Waters, L. B. F. M., & Leinert, C. 2003, *A&A*, 412, L43
- Reipurth, B., Pedrosa, A., & Lago, M. T. V. T. 1996, *A&AS*, 120, 229
- Reipurth, B., & Pattersson, B. 1993, *A&A*, 267, 439
- Rydgren, A. E. 1980, *AJ*, 85, 438
- Saffé, C., Randich, S., Mardones, D., Caselli, P., Persi, P., & Racca, G. 2003, *A&A*, 409, 993
- Sahu, M., & Sahu, K. C. 1992, *A&A*, 259, 265
- Sartori, M. J., Lépine, J. R. D., & Dias, W. S. 2003, *A&A*, 404, 913
- Servoin, J. L., & Piriou, B. 1973, *Phys. Status Solidi B*, 55, 677
- Sitko, M. L., Grady, C. A., Lynch, D. K., Russell, R. W., & Hanner, M. S. 1999, *ApJ*, 510, 408
- Strom, K. M., Strom, S. E., Edwards, S., Cabrit, S., & Skrutskie, M. F. 1989, *AJ*, 97, 1451
- The, P. S., de Winter, D., & Perez, M. R. 1994, *A&AS*, 104, 315
- Thi, W. F., et al. 2001, *ApJ*, 561, 1074
- Toon, O. B., & Ackerman, T. P. 1981, *Appl. Optics*, 20, 3657
- Torres, G., Guenther, E. W., Marschall, L. A., Neuhäuser, R., Latham, D. W., & Stefanik, R. P. 2003, *AJ*, 125, 825
- van Boekel, R., Min, M., Waters, L. B. F. M., de Koter, A., Dominik, C., van den Ancker, M. E., & Bouwman, J. 2005, *A&A*, 437, 189
- van Boekel, R., Waters, L. B. F. M., Dominik, C., Bouwman, J., de Koter, A., Dullemond, C. P., & Paresce, F. 2003, *A&A*, 400, L21
- van den Ancker, M. E., de Winter, D., & Tjin A Djie, H. R. E. 1998, *A&A*, 330, 145
- van den Ancker, M. E., The, P. S., Tjin A Djie, H. R. E., Catala, C., de Winter, D., Blondel, P. F. C., & Waters, L. B. F. M. 1997, *A&A*, 324, L33
- van Dishoeck, E. F. 2004, *ARA&A*, 42, 119
- Waelkens, C., et al. 1996, *A&A*, 315, L245
- Webb, R. A., Zuckerman, B., Platais, I., Patience, J., White, R. J., Schwartz, M. J., & McCarthy, C. 1999, *ApJ*, 512, L63
- Wooden, D. H. 2002, *Earth Moon Planets*, 89, 247
- Zubko, V. G., Mennella, V., Colangeli, L., & Bussoletti, E. 1996, *MNRAS*, 282, 1321